Controls on the geometry and evolution of thin-skinned fold-thrust belts, and applications to the Makran accretionary prism and Indo-Burman Ranges

Thomasina V. Ball[1,2*], Camilla E. Penney[3], Jerome A. Neufeld[1,2,4], Alex C. Copley[3]

[1] *Bullard Laboratories, Department of Earth Sciences, University of Cambridge, Madingley Road, Cambridge, CB3 0EZ, UK*

[2] *BP Institute, University of Cambridge, Madingley Road, Cambridge, CB3 0EZ, UK*

[3] *COMET, Bullard Laboratories, Department of Earth Sciences, University of Cambridge, Madingley Road, Cambridge, CB3 0EZ, UK*

[4] *Department of Applied Mathematics and Theoretical Physics, University of Cambridge, CMS Wilberforce Road, Cambridge, CB3 0WA, UK*

SUMMARY

The formation of fold-thrust belts at convergent margins is a dynamic process. Accretion of weak sediments to the front of the overriding plate results in crustal thickening and continued flexural subsidence of the underthrusting plate. Fold-thrust belts are often treated as a Coulomb wedge having self-similar geometries with a critical taper, and either a rigid or isostatically compensated base. In this paper we build upon this work by developing a new dynamic model to investigate both the role of the thickness and material properties of the incoming sediment, and the flexure in the underthrusting plate in controlling the behaviour and evolution of fold-thrust belts. Our analysis shows that the evolution of fold-thrust belts can be dominated

by either gravitational spreading or vertical thickening, depending on the relative importance of sediment flux, material properties and flexure. We apply our model to the Makran accretionary prism and the Indo-Burman Ranges, and show that for the Makran flexure must be considered in order to explain the dip of the sediment-basement interface from seismic reflection profiles. In the Indo-Burman Ranges, we show that incoming sediment thickness has a first-order control on the variations in the characteristics of the topography from north to south of the Shillong Plateau.

Key words: Continental margin: convergent; Lithospheric flexure; Dynamics: gravity and tectonics; Mechanics, theory and modelling

1   INTRODUCTION

A wide range of geometries of mountain ranges are formed by plate convergence. The sizes and thermal structures of these ranges control their rheology, and therefore their deformation and evolution. At one extreme, the largest ranges on Earth (e.g. the Tibetan Plateau and the Andes) involve the entire thickness of the lithosphere, are bounded by rigid plates that are thousands of kilometres apart, and involve a range of deformation mechanisms including seismic failure in earthquakes and thermally-activated creep (e.g. Brace and Kohlstedt 1980; Chen and Molnar 1983). Opinion is divided in terms of the relative dynamical importance of brittle deformation on faults and the more distributed deformation in the underlying ductile lithosphere, and in the choice of boundary conditions used on the base and lateral edges for models of mountain ranges (e.g. Molnar and Tapponnier 1975; England and McKenzie 1982; Beaumont et al. 2001; Meade 2007; Flesch et al. 2018). In this paper we examine the behaviour of smaller ranges over length scales of 100's km. At some convergent margins weak sediments on an underthrusting plate are deformed during accretion to the front of a relatively rigid 'backstop', which represents a region of the overlying plate that is stronger than the incoming sediments. This leads to the formation of a fold-thrust belt, or an accretionary wedge, which is our focus here.

We examine a coupled system of deformation of the incoming sediment pile and flexure of the underthrusting plate. By developing new dynamic models, we are able to address the role that is played by the thickness and material properties of the incoming sediments, and

⋆ tvb21@cam.ac.uk

⁴⁶ by the elastic properties of the underthrusting plate, in the behaviour and evolution of fold-

⁴⁷ thrust belts. Firstly we describe the effects of changing these physical parameters on the

⁴⁸ geometry and deformation of the resulting fold-thrust belts. We then describe applications to

⁴⁹ specific regions that demonstrate the geological implications of the effects we have studied. In

⁵⁰ particular, we consider the Makran accretionary prism in order to demonstrate the necessity

⁵¹ of including flexure in the model. We then investigate how changing the sediment thickness

⁵² affects the geometry of fold-thrust belts by considering the Indo-Burman Ranges.

⁵³ 2 PREVIOUS MODELS

⁵⁴ Price (1973) was the first to model a wedge-like fold-thrust belt using a continuum plastic

⁵⁵ rheology where the yield strength is depth independent. In Price's model flow is driven by

⁵⁶ horizontal pressure gradients associated with surface slopes. The continuum plastic model

⁵⁷ was revisited by Elliot (1976) and Chapple (1978). By setting the strength of the interface

⁵⁸ between the wedge and the rigid underthrusting plate to be that of the wedge, Elliot (1976)

⁵⁹ showed that the gravitational force provided by the weight of the accreted sediment dominated

⁶⁰ the deformation. Conversely, by introducing a weaker interface between the wedge and the

⁶¹ underthrusting plate, Chapple (1978) highlighted that horizontal compression associated with

⁶² shortening can contribute to overcoming the resisting shear stress at the base of the wedge

⁶³ without the requirement of a surface slope. The analysis of Elliot (1976) and Chapple (1978)

⁶⁴ was then expanded by Stockmal (1983) using slipline theory to calculate the stress and velocity

⁶⁵ field within the wedge.

⁶⁶   Such models do not reflect that the material strength in a fold-thrust belt is expected to

⁶⁷ increase with depth due to the increasing effective overburden stress and lithification. Davis

⁶⁸ et al. (1983); Dahlen et al. (1984) and Dahlen (1984, 1990) used a Coulomb rheology, where

⁶⁹ the yield strength increases with depth and is set by the internal friction angle, for the case of

⁷⁰ a non-cohesive (Davis et al. 1983) or a cohesive (Dahlen et al. 1984) thrust belt. Extensions

⁷¹ to these models have considered the effect of pore fluid pressures and changes in cohesion due

⁷² to compaction and lithification (Zhao et al. 1986). In particular, Dahlen (1984) presented an

⁷³ exact solution for the stress state in a non-cohesive wedge.

⁷⁴   The Coulomb wedge described by Davis et al. (1983) and others relies on the hypothesis

⁷⁵ that the interior of the wedge is everywhere on the verge of failure (Mandl 1988). Hence, this

⁷⁶ model does not account for the possibility that deformation may be confined to a narrow

⁷⁷ zone, as observed in many fold-thrust belts where deformation is dominated by large slip on

⁷⁸ a few major faults (Suppe 1980). Numerical models have been developed by others to allow

for inhomogeneous deformation with more complex rheologies, including plastic (Borja and Dreiss 1989; Willett 1992), elasto-plastic (Simpson 2011), and elasto-visco-plastic (Stockmal et al. 2007; Ruh et al. 2012) rheologies, as well as for time-dependent stress states (e.g. Wang 2006).

Alongside these studies, fold-thrust belts have been described with more simplified rheologies. In thick layers of sediment, deformation is thought to be associated with diffusion creep due to water assisted transport of material via diffusion at the grain scale, and is known to occur at low temperatures in sediments (Rutter 1983). Such a deformation mechanism would result in a viscous fluid rheology at large scales. Emerman and Turcotte (1983) first considered the geometry of a fold-thrust belt with a purely viscous rheology. By using lubrication theory (flow in a thin viscous layer), they described a quasi-steady profile due to the balance of advection of the incoming sediment layer and gravitational spreading within the wedge. Applying the model to bathymetric profiles across the Kurile, Ryukyu and Aleutian accretionary prisms, Emerman and Turcotte inferred sediment viscosities of between $10^{17} - 10^{18}$ Pas. A viscous rheology has also been used to investigate the asymmetry of doubly vergent orogens (Medvedev 2002), and to understand the length scales over which coupling to the kinematics of the underlying mantle is important (Ellis et al. 1995). More recently, Perazzo and Gratton (2010) demonstrated that the growth of fold-thrust belts is self-similar and showed good comparisons to locally averaged profiles of a variety of mountain ranges.

Much of these analyses have either focused on a prescribed taper of the underthrusting plate (Davis et al. 1983; Dahlen et al. 1984) or assumed isostatic compensation (Ellis et al. 1995). However, over smaller length scales of 10's to 100's km, flexure of the underthrusting plate plays an important role in determining the geometry of the resultant deformation (Forsyth 1985; McKenzie and Fairhead 1997), and should therefore be included for a full description of the fold-thrust belt evolution. Many studies have demonstrated that the patterns of gravity anomalies in the forelands of mountain ranges reveal the elastic flexure of the underthrusting plate in response to the load imposed by the mountain range (e.g. Karner and Watts 1983; Lyon-Caen and Molnar 1983; Jordan and Watts 2005; Haddad and Watts 1999; Burov et al. 1990; Snyder and Barazangi 1986; Watts et al. 1995). These studies have been concerned with using the present-day pattern of gravity anomalies to infer the flexural properties of the lithosphere. More recently, numerical models have been used to consider the growth and evolution of the coupled system of flexure in the underthrusting plate overlain by shortening and thickening to form a fold-thrust belt. In particular, studies have focused on coupling flexure with complex rheologies such as an elasto-visco-plastic wedge (Simpson 2006,

113 2010; Stockmal et al. 2007) and a Coulomb wedge (Wang 2001). However, a simplified model

114 combining wedge deformation with flexure in the underthrusting plate is yet lacking.

115   In the next section we build on this previous work by considering the growth of a fold-

116 thrust belt in which the underthrusting plate deforms elastically in response to the evolving

117 overlying fold-thrust belt. We consider a purely viscous rheology to model the long wave-

118 length topography associated with fold-thrust belts on length scales much larger than indi-

119 vidual faults (England and McKenzie 1982). This rheology is chosen for its simplicity, and

120 ability to accommodate distributed and spatially variable deformation, and is appropriate if

121 a large proportion of the deformation is by fluid-activated or thermally-activated creep mech-

122 anisms (Rutter 1983). The low to absent rates of seismicity in the regions to which we apply

123 our model may support this assumption (see below). In section 5.3 we will compare the results

124 of our viscous model to that of a Coulomb wedge model.

3   MODEL SETUP

126 We consider a two-dimensional model of a fold-thrust belt as shown in Fig. 1. Incoming

127 sediment is modelled as a viscous fluid with density ρ, and viscosity η, and the underlying

128 mantle below as an inviscid fluid with density ρ_m. (For a submarine wedge, ρ should be

129 replaced by $\bar{\rho} = \rho - \rho_w$, where ρ_w is the density of water). We take an initial configuration

130 at time $t = 0$ in which the wedge consists of a uniform layer of sediment of thickness T_s.

131 The height $h(x,t)$ is the portion of the wedge above $z = 0$, and $s(x,t)$ is the depth of the

132 interface below $z = 0$, defined as negative in the model. The lateral extent x_N is determined

133 by considering the width of the topography above a threshold value as described in section 4.4.

134 For distances along the x-axis much greater than x_N, the layer is in isostatic balance with the

135 mantle beyond the nose of the thrust belt (see Fig. 1). The underthrusting plate is modelled

136 as a thin elastic beam translating horizontally with speed U towards the backstop, with

137 elastic thickness T_e, Young's modulus E, Poisson's ratio ν, and hence bending stiffness $B =$

138 $T_e^3 E / 12(1 - \nu^2)$. The viscous sediment layer is advected with this plate towards the backstop.

139 We define the convergence velocity U as the total rate of motion between the incoming plate

140 and the backstop. The backstop, which is fixed at $x = 0$, represents a region of overlying plate

141 that is stronger than the incoming sediments. Here, we assume that the backstop remains

142 undeformed during the evolution of the thrust belt and prevents any flow of sediment out of

143 the model domain.

144   Geological and geophysical observations show that the typical vertical thickness of a thrust

145 belt is much smaller than the across-strike width, therefore lubrication theory (flow in a thin

viscous layer) can be used to model deformation in the wedge (Schlichting and Shapiro 1979). The rate of change of the thickness of the wedge $(h - s)$ due to advection of sediment and strain within the wedge can be written as an advection-diffusion equation (e.g. Perazzo and Gratton 2008),

$$\frac{\partial}{\partial t}(h - s) = \frac{\rho g}{3\eta}\frac{\partial}{\partial x}\left[(h - s)^3\frac{\partial h}{\partial x}\right] + U\frac{\partial}{\partial x}(h - s). \tag{1}$$

Across the wedge there is a balance between the flexural subsidence of the plate due to the mass of the overlying wedge and the hydrostatic restoring force of the underlying mantle as a result of this subsidence. This balance is defined by the Euler-Bernoulli beam equation (Timoshenko and Woinowsky-Krieger 1959),

$$B\frac{\partial^4 s}{\partial x^4} + \rho_m g s = -\rho g(h - s). \tag{2}$$

We apply boundary conditions by first imposing no flow of sediment through the backstop at $x = 0$,

$$-\frac{\rho g}{3\eta}(h - s)^3\frac{\partial h}{\partial x}\bigg|_{x=0} = U\,(h - s)|_{x=0}. \tag{3}$$

We assume that loading behind the backstop does not affect the deformation of the underthrusting plate and therefore impose a mechanical break in the plate at $x = 0$ by setting the bending moment and shear force to be zero,

$$\frac{\partial^2 s}{\partial x^2}\bigg|_{x=0} = \frac{\partial^3 s}{\partial x^3}\bigg|_{x=0} = 0, \tag{4}$$

respectively. We impose a uniform sediment layer thickness in the far field, which is in isostatic balance with the underlying mantle below,

$$h \to h_\infty, \quad s \to s_\infty = -\frac{\rho}{\rho_m - \rho}h_\infty \quad \text{as} \quad x \to \infty, \tag{5}$$

such that $h_\infty - s_\infty = T_s$ is the far field sediment layer thickness. Finally, far from the loading in the wedge the underthrusting plate is undeformed so that deflections decay,

$$\frac{\partial s}{\partial x} \to 0 \quad \text{as} \quad x \to \infty. \tag{6}$$

There are several natural length and time scales in the problem, with which we determine a universal, non-dimensional problem. In the horizontal, the length scale at which the weight of the wedge begins to dominate over the strength of the plate is defined as the flexural parameter (also known as the elastogravity length scale), which has units of length,

$$l_e = \left(\frac{B}{\Delta\rho g}\right)^{1/4}, \tag{7}$$

where $\Delta\rho = \rho_m - \rho > 0$ is the density difference between the mantle and the sediment in the wedge. By balancing the evolution of the thickness of the wedge with the advection of sediment

176 and strain within the wedge, as described by equation 1, we may write the characteristic
177 vertical height and time scales as

$$H = \left(\frac{3\eta U l_e}{\rho g}\right)^{1/3}, \quad T = \frac{l_e}{U}. \tag{8}$$

179 Hence we can define non-dimensional variables

$$\tilde{h} = \frac{h}{H} \equiv h\left(\frac{\rho g}{3\eta U l_e}\right)^{1/3}, \quad \tilde{x} = \frac{x}{l_e} \quad \text{and} \quad \tilde{t} = \frac{t}{T} \equiv t\frac{U}{l_e}. \tag{9}$$

181   The non-dimensional equations are therefore functions of only two parameters,

$$\lambda = \frac{\rho}{\rho_m - \rho} \equiv \frac{\rho}{\Delta \rho} \quad \text{and} \quad H_\infty = T_s \left(\frac{\rho g}{3\eta U l_e}\right)^{1/3}. \tag{10}$$

183 The density ratio $\lambda = \rho/\Delta\rho$ describes the proportion of the wedge thickness accommodated
184 by downwards deflection of the underthrusting plate in isostatic balance. The parameter H_∞
185 is the ratio of buoyancy forces to the compressive forces, over the length scale of the flexural
186 parameter. H_∞ is therefore equivalent to the Argand number (often expressed as the ratio
187 between the stress from buoyancy to the stress needed to deform the material; England and
188 McKenzie 1982), with the addition of flexural effects.

189   Dropping the hat decoration, the non-dimensional equations can be written as

$$\frac{\partial}{\partial t}(h - s) = \frac{\partial}{\partial x}\left[(h - s)^3 \frac{\partial h}{\partial x}\right] + \frac{\partial}{\partial x}(h - s), \tag{11}$$

$$\frac{\partial^4 s}{\partial x^4} + s = -\lambda h, \tag{12}$$

192 with boundary conditions

$$(h - s)^2 \frac{\partial h}{\partial x} = -1, \quad \frac{\partial^2 s}{\partial x^2} = \frac{\partial^3 s}{\partial x^3} = 0 \quad \text{at} \quad x = 0, \tag{13}$$

$$h \to \frac{H_\infty}{1 + \lambda}, \quad s \to -\frac{\lambda H_\infty}{1 + \lambda}, \quad \frac{\partial s}{\partial x} \to 0 \quad \text{as} \quad x \to \infty. \tag{14}$$

195 The total volume accumulated in the wedge due to advection is given by

$$H_\infty t = \int_0^\infty (h - s - H_\infty)\, \mathrm{d}x. \tag{15}$$

197 This statement of global mass conservation is a direct consequence of local mass conservation
198 and the requirement of zero flow of sediment through the backstop and out of the model
199 domain, given by equation 3. By varying λ and H_∞, the full parameter space can be explored
200 for any properties of the incoming sediment and underthrusting plate.

201   In deriving this model, we have made several assumptions in order to reduce the number
202 of unknown parameters. Firstly, we model the underthrusting plate as a thin elastic beam
203 resting on a fluid mantle. We assume that the time scale over which the wedge evolves is
204 much longer than the viscous relaxation time of the underlying mantle, and shorter than that

of the lithosphere (Walcott 1970; Watts et al. 2013). Secondly, by modelling the sediment as a viscous fluid we assume that the viscosity of the sediment is much smaller than that of the underthrusting plate (Brace and Kohlstedt 1980). Ellis et al. (1995) included the viscosity of the underlying mantle in their analysis when considering crustal thickening at convergent margins, and showed that the coupling to the mantle can be neglected when the wedge is weakly coupled to its base, or when depth of the underlying mantle is large compared with the deflection of the underthrusting plate, as we assume in our model. A basally driven model can then be used, where the underlying mantle is inviscid in comparison to the sedimentary wedge and only provides a hydrostatic restoring force to the wedge.

At the backstop we impose the boundary condition that there is no flow of sediment out of the wedge. It would be relatively straightforward to include the subduction of deformable sediment in the model (Shreve and Cloos 1986). Doing so would not change the qualitative results of the model but would make the analysis more complex. In our analysis to follow we refer to the bottom of the wedge as the underthrusting plate but this should be thought of as the base of the deformable sediment, and we treat lithified sediment that is mechanically coupled to the underthrusting plate as part of the plate. In addition, we also neglect any erosion of the topography, which would generally smooth the topographic surface, but again have no impact on the qualitative results described.

Finally, we assume a Newtonian viscous rheology for the sediment in the thrust belt, meaning that the stress is linearly related to the strain rate. Our model can be extended to a power law rheology. For a power law rheology the stress is proportional to some power of the strain rate, allowing effective viscosities to reduce with increased shear stress. We anticipate that, as for a convergent Newtonian viscous gravity current on a horizontal non-deforming base (Gratton and Perazzo 2009), a power law rheology would give fold-thrust belts with steeper surface gradients and hence imply larger bulk viscosities than the Newtonian equivalent. However, for simplicity, and because diffusion creep results in a Newtonian rheology, we use a Newtonian viscous fluid in our models.

4   MODEL RESULTS

In this section we describe the different regimes of wedge evolution due to the competition between elastic deformation of the underthrusting plate, advection of sediment, and strain within the wedge. We first give a brief overview of the key results and regimes of wedge evolution in section 4.1. Then, in sections 4.2 and 4.3, we derive the analytical results underpinning these model regimes along with examples of the shapes and vertical and horizontal length

238 scales of wedges in each regime. Finally, in section 4.4 we describe the numerical solutions of
239 the fully coupled system to investigate the transition between these regimes.

4.1 Overview of regimes of wedge evolution

241 The wedge evolves from early- to late-time depending on the vertical and horizontal length
242 scales. We define 'early-times' as when the lateral extent of the wedge is much less than
243 the flexural parameter l_e (non-dimensional extent $x_N \ll 1$) and the vertical thickness of
244 the wedge is much less than the incoming non-dimensional sediment height $H_\infty/(1+\lambda) =$
245 $T_s(\rho g/3\eta U l_e)^{1/3}/(1+\lambda)$, where the density ratio $\lambda = \rho/\Delta\rho$. We define 'late-times' as when
246 the lateral extent of the wedge is much greater than the flexural parameter (non-dimensional
247 extent $x_N \gg 1$) and the vertical thickness of the wedge is much greater than the incoming
248 non-dimensional sediment height $H_\infty/(1+\lambda)$. By balancing the sediment flux due to strain
249 within the wedge with the flux due to advection of sediment on the underthrusting plate, we
250 define a critical non-dimensional parameter $\Lambda_C = \pi^{1/2}H_\infty^3/(1+\lambda)$. The evolution of the wedge
251 from early- to late-time depends on the value of this parameter, and describes whether lateral
252 spreading due to strain within the wedge or vertical thickening due to advection of sediment
253 is the dominant mechanism for growth. From now on we will refer to lateral spreading due
254 to strain within the wedge as 'gravitational spreading', where the lateral extent increases
255 due to gravity acting on topography. For a wedge with a low viscosity, high density and
256 thick incoming sediment layer, and an underthrusting plate with a small elastic thickness
257 and convergence velocity (i.e. large critical non-dimensional parameter $\Lambda_C \gg 1$), the initial
258 evolution is predominantly through gravitational spreading, with little vertical thickening
259 due to advection of sediment. In contrast, for a wedge with a high viscosity, low density
260 and thin incoming sediment layer, and an underthrusting plate with a large elastic thickness
261 and convergence velocity (i.e. small $\Lambda_C \ll 1$), the initial evolution is predominantly through
262 vertical thickening due to advection of sediment, with little gravitational spreading.

263 Fig. 2 plots the lateral extent of the wedge x_N against the normalised maximum topo-
264 graphic height at the backstop, $h_0 = h(0,t)$. The points are calculated numerically as described
265 below in section 4.4, where different symbols represent different values of the non-dimensional
266 parameters H_∞ and λ, and hence Λ_C, with increasing time going from the bottom left to
267 the top right of the graph. Fig. 2 is split into four quadrants, as shown by the vertical and
268 horizontal dashed lines, to indicate the four regimes: early-time; intermediate time, gravita-
269 tional spreading dominant; intermediate time, vertical thickening dominant; and late-time.
270 The schematics i–iv in Fig. 2 demonstrate the key scalings for the vertical and horizontal

length scales of the wedge for these regimes from the theoretical analysis described below. The early- and late-time regimes occur in the bottom left and top right-hand quadrants, with scalings represented by schematics i and iv respectively. When Λ_C is large ($\Lambda_C \gg 1$) the wedge grows predominantly by gravitational spreading, hereafter referred to as Path 1. Evolving through this intermediate regime, the numerical solution passes through the bottom right-hand quadrant with scalings represented by schematic Fig. 2ii. However, when the parameter Λ_C is small ($\Lambda_C \ll 1$) the wedge grows predominantly by vertical thickening due to advection of sediment, referred to as Path 2. Evolving through this intermediate regime, the numerical solution passes through the top left-hand quadrant with scalings represented by schematic Fig. 2iii. We will now describe the analytical results underpinning these model regimes along with examples of the size of wedges in each regime.

4.2   Flexural subsidence of the underthrusting plate

The deformation of the underthrusting plate due to the mass of the overlying wedge is dependent on the lateral extent of the sediment load. For small lateral extents, where the sediment has not spread to lengths greater than the flexural parameter l_e (non-dimensional extent $x_N \ll 1$), the loading due to the wedge can be approximated as a point force localised at the position of the backstop $x = 0$. Assuming also that the increase in the thickness of sediment is small compared with the total incoming sediment thickness, $(h-s)-H_\infty \ll H_\infty$, equation 12, describing the flexural subsidence of the plate, reduces to

$$\frac{\partial^4 s}{\partial x^4} + (1+\lambda)s \simeq -\lambda H_\infty. \tag{16}$$

Boundary conditions at the backstop and in the far field can now be applied (equations 13 and 14) with the condition of zero shear force being replaced by the approximation of a point loading force,

$$\left.\frac{\partial^3 s}{\partial x^3}\right|_{x=0} = -\lambda H_\infty t. \tag{17}$$

Hence the deflection of the underthrusting plate for $x_N \ll 1$ is given by

$$s = -\frac{\lambda H_\infty}{1+\lambda}\left[1 + \sqrt{2}(1+\lambda)^{1/4}te^{-mx}\cos mx\right], \tag{18}$$

where $m = (1+\lambda)^{1/4}/\sqrt{2}$. The maximum deflection is $\sqrt{2}\lambda H_\infty t/(1+\lambda)^{3/4}$ with oscillations that decay to the far field deflection $-\lambda H_\infty/(1+\lambda)$, with decay rate and wavelength $1/m$.

When the lateral extent of the sediment load is much greater than the flexural parameter ($x_N \gg 1$), the underthrusting plate can no longer support the topography. The pressure due to the deflection of the plate is now dominated by a balance between the loading of the wedge

302 and the hydrostatic restoring force of the underlying mantle. For large lateral extents, the
303 wedge therefore transitions into isostatic balance where

$$s(x,t) = -\lambda h(x,t), \tag{19}$$

305 except near the nose region, where flexure of the plate remains important on length scales
306 comparable to the flexural parameter.

4.3   Height of topography

4.3.1   Early-time

309 The evolution of the height of the wedge h depends on the relative height of the wedge
310 compared with incoming non-dimensional sediment height $H_\infty/(1+\lambda)$ above $z = 0$. Initially,
311 the height of the wedge is small compared with the height of the advected sediment layer,
312 $h_0 - H_\infty/(1+\lambda) \ll H_\infty/(1+\lambda)$. In addition, the added load of the wedge is insufficient to
313 significantly deform the plate and hence the underthrusting plate remains undeformed with
314 $s \simeq -\lambda H_\infty/(1+\lambda)$. We can therefore linearise the governing equation for the height of the
315 wedge above the far field sediment height. A scaling of equation 11 suggests that initially
316 thickening due to advection is small,

$$\frac{h}{t} \sim \frac{H_\infty^3 h}{x^2} \gg \frac{h}{x} \quad \text{provided} \quad x_N \ll H_\infty^3, \tag{20}$$

318 giving height and extent scales $h - H_\infty/(1+\lambda) \sim H_\infty^{-1/2} t^{1/2}$ and $x_N \sim H_\infty^{3/2} t^{1/2}$. In this limit
319 the topography of the wedge is self-similar. Therefore, we may define the similarity variable
320 $\zeta = x/(4H_\infty^3 t)^{1/2}$ and write $h = H_\infty/(1+\lambda) + t^{1/2} f(\zeta)$, $s \simeq -\lambda H_\infty/(1+\lambda)$, where f is a
321 solution to the non-linear ordinary differential equation

$$\frac{\partial^2 f}{\partial \zeta^2} + 2\zeta \frac{\partial f}{\partial \zeta} - 2f = 0 \quad \Rightarrow \quad f = c_1 \zeta + c_2 \left[\pi^{1/2} \zeta \operatorname{erfc}(\zeta) - \exp(-\zeta^2) \right], \tag{21}$$

323 and c_1, c_2 are constants of integration that need to be determined by applying boundary
324 conditions at the backstop and in the far field. Linearising the boundary conditions (equations
325 13 and 14),

$$H_\infty^2 \left. \frac{\partial h}{\partial x} \right|_{x=0} = -1 \quad \text{and} \quad h(x \to \infty) \to \frac{H_\infty}{1+\lambda}, \tag{22}$$

327 and applying these to the general solution for f (equation 21), then gives an expression for
328 the topographic height of an accretionary wedge in the early-time regime,

$$h = \frac{H_\infty}{1+\lambda} + \frac{2t^{1/2}}{(\pi H_\infty)^{1/2}} \left[\exp\left(-\frac{x^2}{4H_\infty^3 t} \right) - \frac{\pi^{1/2} x}{2(H_\infty^3 t)^{1/2}} \operatorname{erfc}\left(\frac{x}{2(H_\infty^3 t)^{1/2}} \right) \right]. \tag{23}$$

330 This analytical result is shown by Perazzo and Gratton (2008) for a viscous convergent gravity

current on a horizontal, non-deformable base. The maximum topographic height is $H_\infty/(1+\lambda)+2t^{1/2}/(\pi H_\infty)^{1/2}$ which decays monotonically to the far field sediment layer height $H_\infty/(1+\lambda)$, with lateral extent given by $x_N \sim 2H_\infty^{3/2}t^{1/2}$. Equation 23 for the topographic height along with equation 18 for the deflection of the underlying plate defines the early-time regime where lateral extent of the wedge is much less than the flexural parameter l_e and the vertical height is much less than the non-dimensional incoming sediment height $H_\infty/(1+\lambda)$. Applying these bounds ($x_N \ll 1$ and $h_0 - H_\infty/(1+\lambda) \ll H_\infty/(1+\lambda)$) to the scalings from equation 23 gives a time scale for the early-time regime,

$$2H_\infty^{3/2}t^{1/2} \ll 1 \quad \text{and} \quad \frac{2t^{1/2}}{(\pi H_\infty)^{1/2}} \ll \frac{H_\infty}{1+\lambda} \quad \Rightarrow \quad t \ll \min\left\{ \frac{\pi H_\infty^3}{4(1+\lambda)^2}, \frac{1}{4H_\infty^3} \right\}. \tag{24}$$

To indicate when the early-time regime may be appropriate in nature, we consider a wedge with common values of parameters of sediment thickness, viscosity and density $T_s = 4\,\text{km}$, $\mu = 10^{20}\,\text{Pa s}$ and $\rho = 2400\,\text{kg m}^{-3}$ respectively, where the underthrusting plate has an elastic thickness of $T_e = 20\,\text{km}$, Young's modulus $E = 10^{11}\,\text{Pa}$, Poisson's ratio $\nu = 0.25$, and convergence velocity $U = 4\,\text{mm yr}^{-1}$, with an underlying mantle of density $\rho_m = 3300\,\text{kg m}^{-3}$ ($H_\infty = 0.91$, $\lambda = 2.7$). For an age of $t = 0.1\,\text{Myr}$, this gives a maximum topographic height of $\sim 450\,\text{m}$ above the far field sediment height, with lateral extent of $\sim 8\,\text{km}$. From equation 18, the maximum deflection of the plate is $\sim 43\,\text{m}$ with decay rate and wavelength $\sim 54\,\text{km}$. Substituting these parameters into time scale given in equation 24 shows that the conditions for early-time regime behaviour are satisfied provided $t \ll 1$ Myr. Hence these behaviours are not expected to be observed except in the very early stages of wedge growth. On Fig. 2 this early-time regime represents the bottom left-hand quadrant where $x_N \ll 1$ and $h_0 - H_\infty/(1+\lambda) \ll H_\infty/(1+\lambda)$. This example is marked as a red star in the bottom left-hand quadrant of Fig. 2, and is demonstrated by the schematic i.

4.3.2   *Intermediate time: gravitational spreading dominant*

After this early-time regime the wedge can either grow by gravitational spreading or vertical thickening. If the wedge spreads laterally more rapidly than it thickens vertically, referred to as Path 1 (Fig. 2), it can reach an intermediate regime where the lateral extent of the wedge is much greater than the flexural parameter l_e but the vertical height of the wedge is still much less than the non-dimensional sediment height $H_\infty/(1+\lambda)$. Applying these bounds ($x_N \gg 1$ and $h_0 - H_\infty/(1+\lambda) \ll H_\infty/(1+\lambda)$) to the solution for the early-time topographic height, equation 23, gives a condition for evolution along Path 1,

362 $2H_\infty^{3/2}t^{1/2} \sim 1$ and $\dfrac{2t^{1/2}}{(\pi H_\infty)^{1/2}} \ll \dfrac{H_\infty}{1+\lambda}$ $\Rightarrow$ $\Lambda_C \equiv \dfrac{\pi^{1/2}H_\infty^3}{1+\lambda} \gg 1,$ (25)

363 where Λ_C is the critical non-dimensional parameter defined above, the effect of which is

364 described below.

365 Since the lateral extent of the wedge is much greater than the flexural parameter ($x_N \gg 1$),

366 the wedge is in isostatic balance and the deflection of the plate is linearly proportional to the

367 topographic height, given by equation 19. Substituting this expression for the deflection s

368 into equation 11, and carrying out a similar analysis to above, gives an expression for the

369 topographic of a wedge in the intermediate regime evolving along Path 1,

370 $$h = \frac{H_\infty}{1+\lambda} + \frac{2t^{1/2}}{(\pi(1+\lambda)H_\infty)^{1/2}}\left[\exp\left(-\frac{(1+\lambda)x^2}{4H_\infty^3 t}\right) - \frac{(\pi(1+\lambda))^{1/2}x}{2(H_\infty^3 t)^{1/2}}\operatorname{erfc}\left(\frac{(1+\lambda)^{1/2}x}{2(H_\infty^3 t)^{1/2}}\right)\right].(26)$$

371 The maximum topographic height is $H_\infty/(1+\lambda) + 2t^{1/2}/(\pi(1+\lambda)H_\infty)^{1/2}$ which decays mono-

372 tonically to the far field sediment layer height $H_\infty/(1+\lambda)$, with lateral extent given by $x_N \sim$

373 $2H_\infty^{3/2}t^{1/2}/(1+\lambda)^{1/2}$. To demonstrate evolution of a wedge along Path 1, we consider a wedge

374 with sediment thickness, viscosity and density $T_s = 10\,\mathrm{km}$, $\mu = 10^{20}\,\mathrm{Pas}$ and $\rho = 2400\,\mathrm{kg\,m^{-3}}$

375 respectively, where the underthrusting plate has an elastic thickness of $T_e = 20\,\mathrm{km}$, Young's

376 modulus $E = 10^{11}\,\mathrm{Pa}$, Poisson's ratio $\nu = 0.25$ and convergence velocity $U = 4\mathrm{mm\,yr^{-1}}$, with

377 an underlying mantle of density $\rho_m = 3300\,\mathrm{kg\,m^{-3}}$ ($H_\infty = 2.3$, $\lambda = 2.7$). Substituting these

378 values into equation 25 gives critical non-dimensional parameter $\Lambda_C = 5.6 \gg 1$, hence we

379 would expect the wedge to evolve along Path 1. Taking a wedge of age $t = 5\,\mathrm{Myr}$ gives a

380 maximum topographic height of $\sim 1.1\,\mathrm{km}$ above the far field sediment height, maximum de-

381 flection of the plate of $\sim 2.8\,\mathrm{km}$ and a lateral extent of $\sim 120\,\mathrm{km}$. On Fig. 2 this intermediate

382 regime evolving along Path 1 represents the bottom right-hand quadrant where $x_N \gg 1$ and

383 $h_0 - H_\infty/(1+\lambda) \ll H_\infty/(1+\lambda)$. This example is marked as a purple triangle in the bottom

384 right-hand quadrant of Fig. 2, and is demonstrated by the schematic ii. This evolution repre-

385 sents regions where the incoming sediment layer is thick with low viscosity and high density,

386 and the underthrusting plate has a small elastic thickness and small convergence velocity.

387 *4.3.3 Intermediate time: thickening dominant*

388 If the wedge thickens vertically more rapidly than it spreads laterally, it follows an alternative

389 evolution referred to as Path 2. Along this second trajectory the wedge can reach an interme-

390 diate regime where the lateral extent of the wedge is still much less than the flexural parameter

391 but the vertical height of the wedge is much greater than the non-dimensional sediment height

392 $H_\infty/(1+\lambda)$. Applying these bounds ($x_N \ll 1$ and $h_0 - H_\infty/(1+\lambda) \gg H_\infty/(1+\lambda)$) to the

solution for the early-time topographic height, equation 23, gives a condition for evolution along Path 2,

$$2H_\infty^{3/2}t^{1/2} \ll 1 \quad \text{and} \quad \frac{2t^{1/2}}{(\pi H_\infty)^{1/2}} \sim \frac{H_\infty}{1+\lambda} \quad \Rightarrow \quad \Lambda_C \equiv \frac{\pi^{1/2}H_\infty^3}{1+\lambda} \ll 1. \tag{27}$$

Since the vertical height of the wedge is much greater than the non-dimensional incoming sediment height $H_\infty/(1+\lambda)$, the height of the wedge reaches a quasi-static balance where strain driven by lateral pressure gradients, which results in gravitational slumping and hence diffusive behaviour, balances the advection of the sediment layer by the underthrusting plate. The governing equation for the thickness of the wedge (equation 11) simplifies to

$$0 = \frac{\partial}{\partial x}\left[(h-s)^3\frac{\partial h}{\partial x}\right] + \frac{\partial}{\partial x}(h-s). \tag{28}$$

Integrating equation 28, assuming the underthrusting plate remains relatively undeformed $s \simeq -\lambda H_\infty/(1+\lambda)$, and applying boundary conditions at the backstop and at the nose (equations 13 and 14), gives the expression for the topographic height

$$h = -\frac{\lambda H_\infty}{1+\lambda} + \left[H_\infty^3 + 3(x_N - x)\right]^{1/3}. \tag{29}$$

Using the statement of global conservation of mass (equation 15), we find that the lateral extent x_N is the real root of

$$H_\infty\left(\frac{1}{4}H_\infty^3 + x_N + t\right) = \frac{1}{4}(H_\infty^3 + 3x_N)^{4/3}. \tag{30}$$

Equation 29 describes a cube root profile where the topographic height no longer explicitly depends on time (although there is an implicit time dependence through the lateral extent x_N), and hence can be described as quasi-static. For example, consider a wedge with sediment thickness, viscosity and density $T_s = 1$ km, $\mu = 10^{20}$ Pa s and $\rho = 2400\,\mathrm{kg\,m^{-3}}$ respectively, where the underthrusting plate has an elastic thickness of $T_e = 20$ km, Young's modulus $E = 10^{11}$ Pa, Poisson's ratio $\nu = 0.25$ and convergence velocity $U = 4\,\mathrm{mm\,yr^{-1}}$, with an underlying mantle of density $\rho_m = 3300\,\mathrm{kg\,m^{-3}}$ ($H_\infty = 0.23$, $\lambda = 2.7$). Substituting these values into equation 27 gives critical non-dimensional parameter $\Lambda_C = 0.0056 \ll 1$, hence we would expect the wedge to evolve along Path 2. Taking a wedge of age $t = 1$ Myr gives a maximum topographic height of ~ 1.7 km above the far field sediment height, with lateral extent ~ 3.7 km. From equation 18 the maximum deflection of the plate is ~ 110 m with decay rate and wavelength ~ 54 km. On Fig. 2 this intermediate regime evolving along Path 2 represents the top left-hand quadrant where $x_N \ll 1$ and $h_0 - H_\infty/(1+\lambda) \gg H_\infty/(1+\lambda)$. This example is marked as an orange square in the top left-hand quadrant of Fig. 2, and is demonstrated by the schematic iii. This path represents regions where the incoming sediment

424 layer is thin with a high viscosity and low density, and the underthrusting plate has a large

425 elastic thickness and a high convergence rate.

426 *4.3.4   Late-time*

427 Ultimately, the evolution of a wedge along both Path 1 or Path 2 will transition into the

428 late-time regime where the lateral extent of the wedge is much greater than the flexural

429 parameter ($x_N \gg 1$) and the height of the wedge is much greater than the non-dimensional

430 sediment height ($h_0 - H_\infty/(1 + \lambda) \gg H_\infty/(1 + \lambda)$). Since the lateral extent is much greater

431 than the flexural parameter ($x_N \gg 1$) the wedge is in isostatic balance with deflection given

432 by equation 19. As in the intermediate regime along Path 2, the wedge is in a quasi-static

433 state where strain balances the advection of the sediment layer by the underthrusting plate.

434 Substituting the deflection (equation 19) into the governing equation for the quasi-static wedge

435 (equation 28), integrating and applying boundary conditions at the backstop and the nose

436 (equations 13 and 14), the topographic height is given by

$$437 \quad h = \left[\frac{H_\infty^3}{(1 + \lambda)^3} + \frac{3(x_N - x)}{(1 + \lambda)^2} \right]^{1/3}. \tag{31}$$

438 Again, using the statement of global conservation of mass (equation 15), we find the lateral

439 extent x_N is the real root of

$$440 \quad H_\infty \left(\frac{H_\infty^3}{4(1 + \lambda)} + x_N + t \right) = \frac{1}{4(1 + \lambda)} (H_\infty^3 + 3(1 + \lambda)x_N)^{4/3}. \tag{32}$$

441 Equation 31 describes a cube root profile where the topographic height of the wedge no longer

442 explicitly depends on time (although there is an implicit time dependence through the lateral

443 extent x_N). For example, consider a wedge with sediment thickness, viscosity and density

444 $T_s = 2\,\text{km}$, $\mu = 10^{19}\,\text{Pa s}$, $\rho = 2400\,\text{kg m}^{-3}$ respectively, where the underthrusting plate has an

445 elastic thickness of $T_e = 20\,\text{km}$, Young's modulus $E = 10^{11}\,\text{Pa}$, Poisson's ratio $\nu = 0.25$ and

446 convergence velocity $U = 20\,\text{mm yr}^{-1}$, with an underlying mantle of density $\rho_m = 3300\,\text{kg m}^{-3}$

447 ($H_\infty = 0.57$, $\lambda = 2.7$). For an age of $t = 20\,\text{Myr}$, the wedge would have maximum topographic

448 height $\sim 2.3\,\text{km}$ above the far field height, maximum deflection of the plate of $\sim 6.3\,\text{km}$,

449 with lateral extent $\sim 130\,\text{km}$. On Fig. 2 this late-time regime represents the top right-hand

450 quadrant where $x_N \gg 1$ and $h_0 - H_\infty/(1 + \lambda) \gg H_\infty/(1 + \lambda)$. This example is marked as a

451 pink diamond in the top right-hand quadrant of Fig. 2, and is demonstrated by the schematic

452 iv.

453 The analytical solutions derived above describe the limiting case in each of the four regimes

454 shown in Fig. 2. However, a given fold-thrust belt will lie along an evolutionary transition

455 between these solutions. In order to fully understand how a fold-thrust belt evolves, in the next

456 section we solve this coupled system numerically. In particular, we describe the full evolution

457 of two wedges, one evolving along Path 1, and one evolving along Path 2.

4.4　Numerical solutions

459 We solve the coupled system of non-dimensional equations for the evolution of the topographic

460 height and the flexural subsidence of the underthrusting plate given by equations 11 and 12

461 along with boundary conditions at the backstop and in the far field (equations 13 and 14),

462 and global mass conservation (equation 15). The numerical scheme uses a finite difference

463 Crank-Nicolson algorithm with an adaptive time and spatial step, and a predictor-corrector

464 scheme to handle the non-linearities.

465 　　Fig. 2 plots the vertical topographic height against the lateral extent for seven different

466 numerical simulations with different values of non-dimensional parameters H_∞ and λ (see

467 legend inset). Note that the location of the lateral extent x_N is determined by considering

468 the width of topography above a threshold value such that $h(x_N, t) - H_\infty/(1 + \lambda) = 10^{-3}$ at

469 the edge of the wedge, consistent in all simulations. The transition between evolution along

470 Path 1 or Path 2 depends on the critical non-dimensional parameter $\Lambda_C = \pi^{1/2} H_\infty^3/(1 + \lambda)$.

471 Fig. 2 shows that by decreasing Λ_C the evolution moves from Path 1 to Path 2 with the

472 transition occurring when $\Lambda_C \sim 1$. In dimensional form, the transition occurs when $\Lambda_C =$

473 $\pi^{1/2} T_s^3 \rho g/(3\eta U l_e (1 + \rho/\Delta\rho)) \sim 1$. Hence, by decreasing the sediment thickness and density

474 and/or increasing the sediment viscosity and elastic thickness and convergence velocity of the

475 underthrusting plate, evolution moves from predominantly gravitational spreading along Path

476 1 to predominantly vertical thickening along Path 2.

477 　　We now describe in more detail the two numerical simulations with the largest and small-

478 est values of Λ_C. Fig. 3a plots the profiles of the topographic height (blue lines) and plate

479 deflection (red lines) with parameters $H_\infty = 3.2$, $\lambda = 3.0$ and $\Lambda_C = 14.5 \gg 1$ for times

480 $t = 5 \times 10^{-4}$, 10^{-3},..., 10^2, where Fig. 3b (inset) is a zoom of profiles at early times ($t \leq 10^{-1}$).

481 Evolution of the wedge is along Path 1, where gravitational spreading dominates over vertical

482 thickening. Fig. 3c is a log-log plot of the maximum topographic height (blue squares) and

483 maximum plate deflection (red triangles) against time. The dotted and dashed lines plot the

484 early- and late-time solutions respectively for the maximum topographic height (blue, equa-

485 tions 23 and 31) and the maximum plate deflection (red, equations 18 and 19) and show good

486 agreement with the numerical solution for small and large times. The green dashed line plots

487 the solution between the early- and late-times for the height of the topographic wedge, defined

488   as the intermediate solution, for evolution along Path 1 (equation 26). Although it does well

489   to describe the points around $t \sim 1$, the intermediate solution largely overlaps the early-time

490   and late-time solutions and hence does not provide any further information about the growth

491   of the wedge. However, we would anticipate this solution to be more useful (i.e. describe the

492   evolution when both the early- and late-time do not apply) when there is a larger separation

493   between the early- and late-time i.e. for larger Λ_C. This evolution describes a wedge with

494   a thick incoming sediment layer of large density and small viscosity, and an underthrusting

495   plate with a small elastic thickness and low convergence velocity.

496   Fig. 3d plots the profiles of the topographic height (blue lines) and plate deflection

497   (red lines) with parameters $H_\infty = 0.4$, $\lambda = 3.0$ and $\Lambda_C = 0.03 \ll 1$ for times $t = 5 \times$

498   $10^{-4}, 10^{-3},...,10^2$, where Fig. 3e (inset) is a zoom of profiles at early times ($t \leq 1$). Evo-

499   lution of the wedge is along Path 2, where vertical thickening dominates over gravitational

500   spreading. Fig. 3f is a log-log plot of the maximum topographic height (blue squares) and

501   maximum plate deflection (red triangles) against time. The dotted and dashed lines plot the

502   early- and late-time solutions respectively for the maximum topographic height (blue, equa-

503   tions 23 and 31) and the maximum plate deflection (red, equations 18 and 19) and again shows

504   good agreement with the numerical solution for small and large times. The green dashed line

505   plots the solution between early- and late-times for the height of the topographic wedge (the

506   intermediate solution) for the evolution along Path 2 (equation 29). This intermediate solu-

507   tion does well to describe the points around $t \sim 1$ where both the early-time and late-time

508   solution do not apply: the numerical solution given by the blue squares sits in between the

509   blue dot-dashed and dashed lines for the early- and late-time solutions respectively, but sits

510   very close the green dashed line of the intermediate solution. This evolution describes a wedge

511   with a thin incoming sediment layer of small density and large viscosity, and an underthrust-

512   ing plate with a large elastic thickness and high convergence velocity. Comparing the profiles

513   of the two wedges (Figs 3a,d) there is a clear difference in the nose region of the wedge where

514   there is a prominent flexural depression and bulge when $\Lambda_C = 0.03 \ll 1$ compared with when

515   $\Lambda_C = 14.5 \gg 1$. This forms at early times, Fig. 3e, and then propagates as a steady structure

516   at the nose, Fig. 3d. This flexural depression and bulge demonstrates that, even at late times

517   when the wedge is in isostatic balance, flexure remains important on length scales compa-

518   rable with the flexural parameter l_e. Away from the nose, the general shape of the profiles

519   look similar, however the underlying balance of forces changes significantly between the two

520   regimes, from gravitational spreading dominant to advection dominant, which is what defines

521   the 'regimes'.

5   DISCUSSION AND APPLICATIONS

The model described above considers how changing the properties of the wedge (density, viscosity, age, incoming sediment thickness) and properties of the underthrusting plate (elastic thickness, convergence velocity) affect the evolution of the wedge. We now discuss the effects of changing two key parameters: the incoming sediment thickness T_s and elastic thickness T_e.

Fig. 4 shows the evolution of a wedge in $5\,\mathrm{Myr}$ intervals for $t = 5 - 50\,\mathrm{Myr}$, convergence velocity $U = 4\,\mathrm{mm\,yr^{-1}}$, viscosity $\eta = 10^{20}\,\mathrm{Pas}$, sediment and underlying mantle densities $\rho = 2400\,\mathrm{kg\,m^{-3}}$, $\rho_m = 3300\,\mathrm{kg\,m^{-3}}$ (density ratio $\lambda = 2.7$). Figs 4a–c show a wedge in isostatic balance for which we neglect the elastic thickness of the plate ($T_e = 0\,\mathrm{km}$) with increasing sediment thicknesses $T_s = 2$, 4 and $10\,\mathrm{km}$. Figs 4d–f show the evolution of an identical series of wedges now resting on a underthrusting plate with an increased elastic thickness of $T_e = 20\,\mathrm{km}$ (Young's Modulus $E = 10^{11}\,\mathrm{Pa}$ and Poisson's ratio $\nu = 0.25$). Substituting these values into the critical non-dimensional parameter Λ_C gives $\Lambda_C = 0.045$, 0.36 and 5.6 for corresponding incoming sediment thicknesses $T_s = 2$, 4 and 10 km. Hence, both Fig. 4 and the values of Λ_C demonstrate that, as described in the previous section, decreasing the incoming sediment thickness causes the evolution to transition from Path 1 (Fig. 4f), to Path 2 (Fig. 4d; decreasing Λ_C), where vertical thickening dominates over gravitational spreading.

For the smallest sediment thickness, $T_s = 2\,\mathrm{km}$ in Figs 4a and 4d, increasing the elastic thickness gives profiles with a higher maximum topographic elevation for small lateral extents. This is consistent with a stronger plate providing additional support to topography. In addition, increasing the elastic thickness gives a shallower dip to the deflection of the underthrusting plate behind the nose of the wedge, with a flexural depression and bulge in front of the nose of the wedge, see Figs 4d and 4e. This feature is present because flexure becomes important when topography varies on length scales comparable with the flexural parameter l_e, for example near the nose. As the incoming sediment thickness increases the elastic thickness of the plate has less of an impact on the profiles. This effect is clearly shown in Figs 4c and 4f for $T_s = 10\,\mathrm{km}$ where the profiles of the wedge for the isostatic and flexural case are almost identical. By increasing the incoming sediment thickness, the critical non-dimensional parameter Λ_C increases causing the transition to isostatic balance to occur at earlier times. Hence, we would expect that changing the elastic thickness would have less of an impact for wedges with larger sediment thicknesses.

In order to examine the effects described in our model, we now consider the Makran accretionary prism and the Indo-Burman Ranges. In the analysis we will refer to specific values of the incoming sediment thickness, viscosity and density, and the elastic properties

556 and convergence velocity of the underthrusting plate. However, the aim is to illustrate the
557 importance of flexure and incoming sediment thickness on the evolution of fold-thrust belts
558 in general, rather than to imply these ranges are particularly unusual.

5.1 Makran accretionary prism

560 The Makran accretionary prism, Fig. 5a, is one of the largest accretionary wedges on Earth.
561 With a large sediment thickness on the incoming plate of $\sim 7\,\text{km}$ (Kopp et al. 2000; White
562 1982), the Makran accretionary prism is formed due to the subduction of the Arabian plate
563 beneath southern Iran and Pakistan. The convergence rate between Arabia and eastern
564 Iran/western Pakistan varies from $19.5 \pm 2\,\text{mm}\,\text{yr}^{-1}$ in the west to $27 \pm 2\,\text{mm}\,\text{yr}^{-1}$ in the
565 east (Vernant et al. 2004). Accretion of sediment into the wedge is thought to have started
566 in the Eocene (Byrne et al. 1992), however an imbricate zone of upper Cretaceous rocks have
567 been identified in the northern part of the Makran (Dolati 2010), which may represent the
568 onset of sediment accretion. These observations give a possible age range for the onset of
569 growth of the accretionary wedge of $30 - 90\,\text{Myr}$.

570   Fig. 5b shows three topographic profiles across the Makran centered on 59.5ºE, 61ºE
571 and 63ºE (red, green and blue lines respectively). The profiles show a negligible along-strike
572 change in topography suggesting a two-dimensional model is appropriate. Fig. 5c plots the
573 sediment-basement interface from seismic reflection profiles at 62.9ºE (solid black line, Kopp
574 et al. 2000). The blue dots plot the inferred subduction interface at 62ºE (Penney et al. 2017)
575 based on the location of earthquakes interpreted as occurring on the subduction interface or
576 within the subducting plate. In the following comparisons, we take the middle topographic
577 profile at 61ºE (as there is negligible along strike variation) along with the sediment-basement
578 and plate interface datasets shown in Fig. 5c. We assume the backstop of the wedge is located
579 roughly at 27.5ºN based on the location of the Jaz Murian and Maskel depressions, which
580 low elevations and low seismic strain rates suggest are relatively undeformed. However, we
581 will show that the position of the backstop only affects the age of the wedge in the numerical
582 simulations, and not our overall conclusions regarding the controls on the evolution of the
583 wedge.

584   We consider the effects of flexure in the Makran accretionary prism by calculating two
585 models with different elastic thicknesses, but with the same incoming sediment thickness,
586 viscosity and density, underlying mantle density, and underthrusting plate convergence rate.
587 First we consider a flexural model with incoming sediment thickness $T_s = 7 \pm 1\,\text{km}$, con-
588 vergence velocity $U = 25 \pm 5\,\text{mm}\,\text{yr}^{-1}$ and mantle density $\rho_m = 3300\,\text{kg}\,\text{m}^{-3}$. We then find

an elastic thickness, viscosity, density and age that best reproduces the observed topography and sediment-basement interface from 195 numerical simulations for different values of non-dimensional sediment thickness H_∞. For all input parameters, we failed to reproduce observations from the Makran accretionary prism for small sediment densities, suggesting significant sediment compaction. Hence, we take a higher estimate of $\lambda = 5.0$, $\rho = 2750\,\mathrm{kg\,m^{-3}}$.

For the range of sediment thicknesses and convergence rates, we find a good fit to the observations for an elastic thickness of $T_e = 18 - 24\,\mathrm{km}$ (flexural parameter $l_e = 56 - 69\,\mathrm{km}$) with incoming sediment viscosity $\eta = 0.9 - 1.5 \times 10^{20}\,\mathrm{Pa\,s}$ and an age of between $t = 44 - 66\,\mathrm{Myr}$, given by parameters $H_\infty = 0.68 - 0.95$, $\Lambda_C = 0.094 - 0.25$. A comparison between the numerical simulation and the observations for $T_s = 7\,\mathrm{km}$ and $U = 25\,\mathrm{mm\,yr^{-1}}$ is plotted in Fig. 6c giving $T_e = 20\,\mathrm{km}$, $\eta = 1.1 \times 10^{20}\,\mathrm{Pa\,s}$ and $t = 42\,\mathrm{Myr}$. The critical non-dimensional parameter $\Lambda_C = \pi^{1/2} H_\infty^3/(1 + \lambda) = 0.094 - 0.25 \ll 1$ suggests that the Makran accretionary prism evolved along Path 2 where vertical thickening was the dominant growth mechanism, although testing this hypothesis would require tectonic reconstructions beyond the scope of the present study. The lateral extent and topographic height of the Makran accretionary prism are plotted on the regime plot in Fig. 2 given by the black hexagram labelled 'M' and shows that the Makran is now in the late-time regime. As a result, only the nose region of the sediment-basement interface, where flexure is important, can constrain the elastic thickness. Therefore, a wide range of elastic thicknesses, $T_e = 18 - 24\,\mathrm{km}$, can fit the observations. Such elastic thicknesses are consistent with previous studies on the elastic thickness of the Arabian plate in the Makran zone (Chen et al. 2015), and with observed elastic thicknesses for oceanic lithosphere elsewhere (Craig and Copley 2014). Our estimate of the sediment viscosity is slightly higher than estimated previously in some studies (Shreve and Cloos 1986; Emerman and Turcotte 1983) but similar to other recent studies of viscous wedges (Medvedev 2002; Copley and McKenzie 2007). Finally, the estimated age of $t = 44 - 66\,\mathrm{Myr}$ is consistent with the geology but is primarily a function of the choice of location of the backstop, and hence volume of sediment accumulated in the wedge. As the wedge is in the late-time regime, the topographic height and plate deflection are given by equations 31 and 19, which do not explicitly depend on time, although there is an implicit time dependence through lateral extent x_N. As a result, the choice of backstop location determines the age of the wedge but not any other parameters in the model.

The second model we consider is in isostatic balance ($T_e = 0\,\mathrm{km}$), but otherwise has the same parameter values as the model described above. Fig. 6a plots the numerical profiles for the topographic height and base of the sediment with elastic thicknesses $T_e = 0\,\mathrm{km}$ in

isostatic balance (solid red lines) and $T_e = 20 \, \text{km}$ (solid blue lines) for $t = 10, 20, 30, 40$ and $50 \, \text{Myr}$. The topography is almost identical in the two models, apart from the flexural depression and bulge at the nose of the wedge observed in the flexural model. However, there is a significant difference between the two models in the depth to the base of the sediment, particularly behind the nose where the dip of the base of the sediment is much more gentle in the flexural model compared with the isostatic model. Figs 6b and 6c then compare these models for $t = 42 \, \text{Myr}$ in each case, with the data for the topographic height and sediment-basement interface (solid black lines with open circles). The topography agrees well in both cases. When considering the base of the sediment, particularly the comparison with the seismic reflection profiles, a flexural model with elastic thickness $T_e = 20 \, \text{km}$ does a better job at reproducing the observed geometry than the purely isostatic model where the elastic thickness is neglected. This result suggests that flexure is necessary to explain the dipping sediment-basement interface as observed in seismic reflection profiles, and hence shows the importance of modelling flexure in the underlying plate.

5.2   Indo-Burman Ranges

The Indo-Burman Ranges were formed by accretion of sediment from the underthrusting Indian plate as it subducts beneath southeast Asia (Ni et al. 1989; Stork et al. 2008; Steckler et al. 2016), see Fig. 7a. The fold-thrust belt is thought to have developed since the late Oligocene (Soibam et al. 2015). Two topographic sections, north and south of the Shillong Plateau (marked as 'SP' in Fig. 7a), are shown in Fig. 7 as blue and red lines. The surface geology within the Indo-Burman Ranges is characterised by progressively older rocks from west to east. South of the Shillong Plateau, sedimentary rocks in the central part of the range are composed of an Eocene sequence ('inner' Indo-Burman wedge), with a western portion of younger rock composed of Neogene fluvio-deltaic sediments and turbidites ('outer' Indo-Burman wedge) (Sikder and Alam 2003; Khin et al. 2014, 2017). The eastern margin of the Indo-Burman Range is characterised by upper-Cretaceous and Triassic deep water sediments, Mesozoic metamorphics and Jurassic ophiolite assemblages (Brunnschweiler 1974; Mitchell 1993). North of the Shillong Plateau, the western portion of the Indo-Burman wedge comprises of an Oligocene sedimentary sequence, with a region towards the east of Cretaceous sandstones overlying mafic volcanics of a Jurassic ophiolite suite (Ghose and Singh 1980; Brunnschweiler 1966). The region of ophiolites and metamorphics that straddle the length of the range is taken to represent a rigid backstop, which allows the fold-thrust belt to form (marked on Fig. 7a, black dashed line; Figs 7b–c, grey shaded region).

Along the Indo-Burman Ranges from north to south of the Shillong Plateau there is a significant change in both foreland sediment thickness and the topography of the wedge. In the north, the Indo-Burman Ranges are bounded to the west by the lowlands of Assam. The sediment thickness ranges from zero, where the crystalline basement is exposed at the surface (e.g. Mikir Hills, marked as 'M' in Fig. 7a), up to $\sim 5\,\mathrm{km}$ (Dasgupta et al. 2000) in the northeastern corner of the syntaxis. The average shown by Dasgupta et al. (2000) is $\sim 2\,\mathrm{km}$. The topography is characterised by a narrow range width and steep surface slopes near the range front, shown as the blue lines on Fig. 7b. South of the Shillong Plateau, the Indo-Burman Ranges are bounded by the Surma Basin (marked as 'SB' in Fig. 7a) and the Bengal Basin, where the sediment thickness in the foreland is significantly larger ($\sim 15 - 22\,\mathrm{km}$; Curray 1991; Alam et al. 2003). The Indo-Burman Range has a larger width and shallower surface slopes than to the north of the Shillong Plateau, shown as red lines on Fig. 7c.

The sedimentary sequences that make up the fold-thrust belt to the west of the backstop in the Indo-Burman Ranges were originally deposited in a series of basins with a common sediment source from the Ganges and Brahmaputra river networks (Steckler et al. 2008; Govin et al. 2018). Hence, we expect the lithology of the sediment in the north and south Indo-Burman wedge to be similar. This similarity suggests that this region may provide insights into the effects of changing sediment thickness on the formation of a fold-thrust belt.

The lower-crustal depth and strike-slip style of earthquakes in the Indo-Burman Ranges suggest they are occurring within the underthrusting Indian plate (Mitra et al. 2005). Hence, the earthquake locations do not constrain the depth of the thrust interface. In the analysis to follow we therefore focus on the geometry of topography in the region, rather than the (unknown) geometry of the underthrusting plate.

The Indo-Burman Ranges have shallower surface slopes and larger range widths where the foreland sediment thickness is larger, south of the Shillong Plateau. This observation is consistent with the effect of increasing sediment thickness shown in Fig. 4. To investigate further, we consider two models in isostatic balance with different incoming sediment thicknesses, but otherwise the same parameter values. We assume isostatic balance as we do not have information about the underthrusting plate needed to constrain the elastic thickness. However, as shown in Fig. 4, the qualitative behaviour of changing sediment thickness is independent of the elastic thickness, and hence this does not affect our conclusions. We consider a range of sediment densities $\rho = 2400 - 2750\,\mathrm{kg\,m^{-3}}$, with mantle density $\rho_m = 3300\,\mathrm{kg\,m^{-3}}$ (density ratio $\lambda = 2.7 - 5.0$). We then find the viscosity, convergence velocity and sediment thicknesses in the north and south that best reproduce the observations of topography. From the estimate

that the formation of the fold-thrust belt started in the Oligocene (Soibam et al. 2015), we take an age of $t = 30 \pm 10$ Myr. However this choice only affects the quantitative parameter values determined, not the qualitative interpretations. For the estimated range of ages and sediment densities, we find incoming sediment thickness in the north of $T_{s(north)} = 2.1 - 2.3$ km and in the south of $T_{s(south)} = 4.7 - 5.0$ km, with sediment viscosity $\eta = 3.0 - 8.8 \times 10^{19}$ Pas and underthrusting plate convergence velocity $U = 2.8 - 8.8$ mm yr^{-1} for both the north and the south.

The estimate of incoming sediment thickness in the north is consistent with the observation that the foreland sediment thickness can range from zero to ~ 5 km in places (Dasgupta et al. 2000) with an average of ~ 2 km. In the south, however, the estimate of $T_{s(south)} = 4.7 - 5.0$ km is significantly less than the observation $\sim 15 - 22$ km from seismic data (Curray 1991; Alam et al. 2003). It has been suggested that temperatures and pressures at large depths in the sediment layer are sufficient for metamorphism to take place (Curray 1991). If this is the case, only the upper deformable portions of the sediment layer may be playing a role in the growth of the wedge. Given that our model estimates the effective deformable sediment thickness, we would expect to underestimate the true sediment thickness, as the deeper parts will be dewatered, lithified, and effectively part of the rigid Indian plate. Crucially, our models reproduce a thicker sediment sequence to the south than north of the Shillong Plateau, consistent with the observations. Sikder and Alam (2003) observe a detachment in seismic reflection data at around 4s two-way travel time, corresponding with a depth of roughly ~ 5 km, which is consistent with more recent studies (Betka et al. 2018), and hence supports our estimate of the effective deformable sediment thickness. The value of sediment viscosity $\eta = 3.0 - 8.8 \times 10^{19}$ Pas is consistent with previous studies on the Indo-Burman Ranges (Copley and McKenzie 2007) and on sediments under similar conditions (Nino et al. 1998; Gratier et al. 1999; Connolly and Podladchikov 2000). Finally, the convergence velocity of $U = 2.8 - 8.8$ mm yr^{-1} is consistent with the total rate of convergence of $5 - 10$ mm yr^{-1} in this area from present-day geodetic data (Steckler et al. 2016), but we note there is a trade-off with estimating the age of the fold-thrust belt, the sediment volume, and changes in either of these quantities through time.

Fig. 8a plots numerical profiles for the topographic height of a wedge with sediment thicknesses $T_{s(north)} = 2.2$ km (solid blue lines) and $T_{s(south)} = 5.0$ km (solid red lines) for $t = 10, 20, 30, 40$ and 50 Myr, with convergence velocity $U = 3.8$ mm yr^{-1}, viscosity $\eta = 5.0 \times 10^{19}$ Pas, and sediment and underlying mantle densities $\rho = 2400$ kg m^{-3}, $\rho_m = 3300$ kg m^{-3}. This comparison again shows that for larger sediment thicknesses, the wedge formed has a

larger range width with a shallower topographic slope. Figs 8b and 8c plot the comparisons between topographic data in the northern and southern part of the Indo-Burman Ranges respectively (solid black lines with open circles) with the numerical profiles for an age of $t = 30\,\text{Myr}$ (blue and red solid lines). By increasing the sediment thickness by more than a factor of two going from the north to the south, the difference in surface slopes and range widths can be reproduced. The discrepancy in Fig. 8b between the back of the wedge in the numerical simulation and the backstop inferred from the geology is due to choosing the same age for the fold-thrust belt in the north and south. However, the mismatch between the observations and the model is small given the uncertainties in the location of the backstop. Our results therefore suggest that the incoming sediment thickness is playing a first-order role in the development of topography in the Indo-Burman Ranges.

5.3   Comparison with Coulomb wedge theory

In our model we use a purely viscous rheology to describe the incoming sediment. As a result of this choice of rheology, the shear stresses are unbound. The shear stress can be written as

$$\tau = \eta \frac{\partial u}{\partial z} = -\rho g \frac{\partial h}{\partial x}(h - z), \tag{33}$$

which is maximum at the base, $z = s$. For example, for the flexural model proposed for the Makran shown in Fig. 6c, the maximum shear stress at the base is $\sim 8\,\text{MPa}$, in agreement with that calculated by Penney et al. (2017) of $\sim 5 - 35\,\text{MPa}$. For the Indo-Burman Ranges, the maximum shear stress is calculated for the base of northern profile, shown in Fig. 8b, to be $\sim 1\,\text{MPa}$. Hence, for both comparisons the shear stress is low, and is consistent with the levels of stress under which rocks can deform at geological strain rates by creep. Unlike Coulomb wedge theory that includes a yield stress, our model does not aim to explain brittle deformation. For a purely viscous rheology, the strain rate is linearly proportional to the shear stress, $\dot{\xi} = \tau/\eta$. Equation 33 shows that the strain rate increases linearly with depth and is proportional to gradients in surface topography. At late-times, the topography of our model wedges exhibit concave-downward profiles with increasing surface gradients towards the toe of the wedge. Hence, we would expect to see the largest strain-rates at depth and towards the toe; a feature analogous to the strain rate pattern for Coulomb wedge theory as described by Willett (1992).

A key feature of Coulomb wedge theory is that everywhere in the interior of the wedge is on the verge of failure by the same mechanism, i.e. thrust faulting at the angle of sliplines. In contrast, our model allows for distributed and spatially variable deformation. The main

distinguishing feature between our viscous model and Coulomb wedge theory is the surface topography of wedges produced. Unlike the linear taper from cohesionless Coulomb wedge theory, a viscous rheology produces a range of topographies from concave-upward to concave-downward as the wedge evolves in time. As seen from the comparisons with the Makran accretionary prism and the Indo-Burman Ranges, these shapes are consistent with observations from a range of locations. However, a clear direction for future work will be to examine the extent to which this is globally true.

6 CONCLUSION

We have presented an analytical and numerical model to describe the growth of a fold-thrust belt due to the accretion of sediments from the underthrusting plate. In particular, we have examined a balance between advection of sediment and gravitational spreading within an accretionary wedge coupled to the flexural subsidence of the underthrusting plate. Our analysis shows that the evolution of accretionary wedges is crucially dependent on two non-dimensional parameters: the non-dimensional sediment thickness $H_\infty = T_s(\rho g/3\eta U l_e)^{1/3}$ and the density ratio $\lambda = \rho/\Delta\rho$, where T_s, ρ, η are the incoming sediment thickness, density and viscosity, U is the convergence rate of the incoming plate, and l_e is the flexural parameter, the length scale at which the weight of the wedge begins to dominate over the strength of the plate. We describe early- and late-time regimes of the wedge and demonstrate two paths of evolution between these regimes, where the wedge either grows predominantly through gravitational spreading (Path 1) or through vertical thickening due to advection of sediment (Path 2) depending on the size of the critical non-dimensional parameter $\Lambda_C = \pi^{1/2}H_\infty^3/(1 + \lambda)$. In addition, we solve the coupled system numerically to understand the transition between these regimes and explore the parameter space more widely.

The generality of our model allows conclusions to be drawn in a multitude of locations. We have considered the particular examples of the Makran accretionary prism and the Indo-Burman Ranges, to investigate the importance of sediment thickness and elastic thickness (flexure of the underthrusting plate) in the growth of a fold-thrust belt. We have shown that flexure is important in the Makran accretionary prism in order to understand dip in the sediment-basement interface from seismic reflections profiles. In the Indo-Burman Ranges, we have shown that a lateral contrast in sediment thickness plays an important role in generating the different styles of topography north and south of the Shillong Plateau.
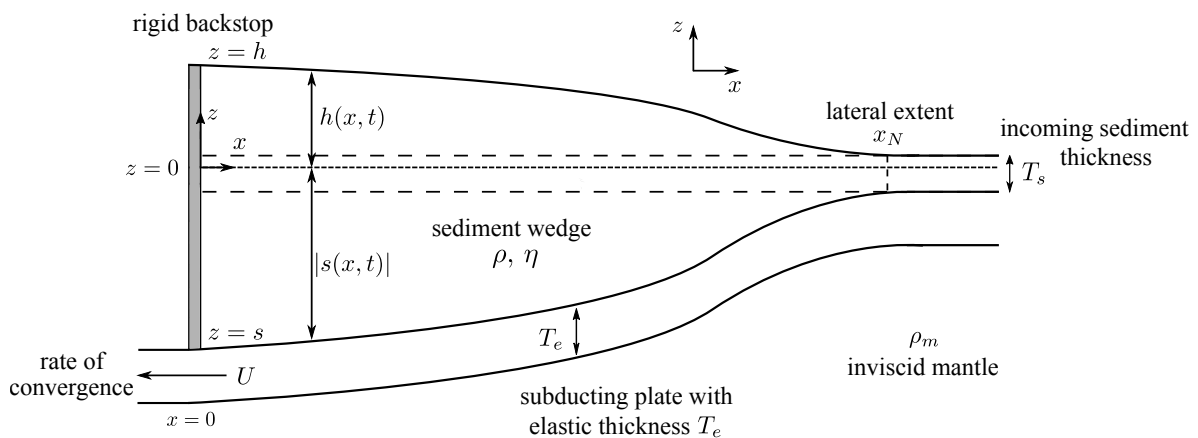
**Figure 1.** Schematic showing the two-dimensional theoretical model for the cross-section of a fold-thrust belt with the physical parameters in the system defined as topographic height h, plate deflection s, lateral extent x_N, incoming sediment thickness T_s, sediment and mantle densities ρ and ρ_m, and viscosity η, and underthrusting plate with elastic thickness T_e and convergence velocity U.
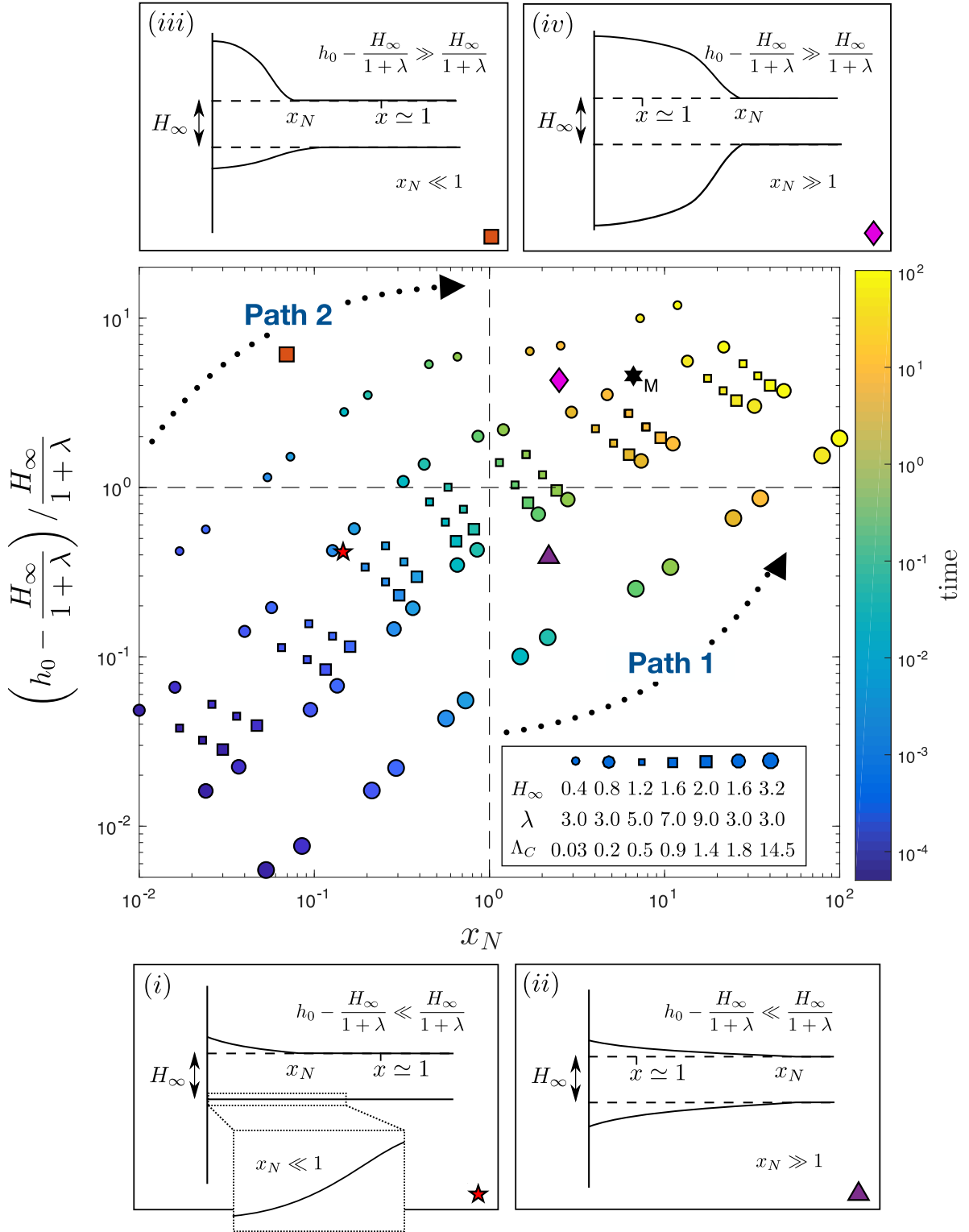
Figure 2. Regime plot. Graph of horizontal extent x_N plotted against maximum vertical topographic height h_0 normalised by the sediment thickness above $z = 0$, $H_\infty/(1+\lambda)$, for seven different numerical simulations for different values of parameters H_∞ and λ, and hence Λ_C, see legend. (i-iv) Schematics of different regimes of propagation: (i) Early-time regime, (ii) intermediate regime along Path 1, where gravitational spreading dominates, (iii) intermediate regime along Path 2, where vertical thickening due to advection of sediment dominates, and (iv) late-time regime. The red star, purple triangle, orange square and pink diamond refer to specific examples of wedges in each regime as described in section 4.3. The black hexagram labelled 'M' refers to the Makran accretionary prism, see section 5.1.
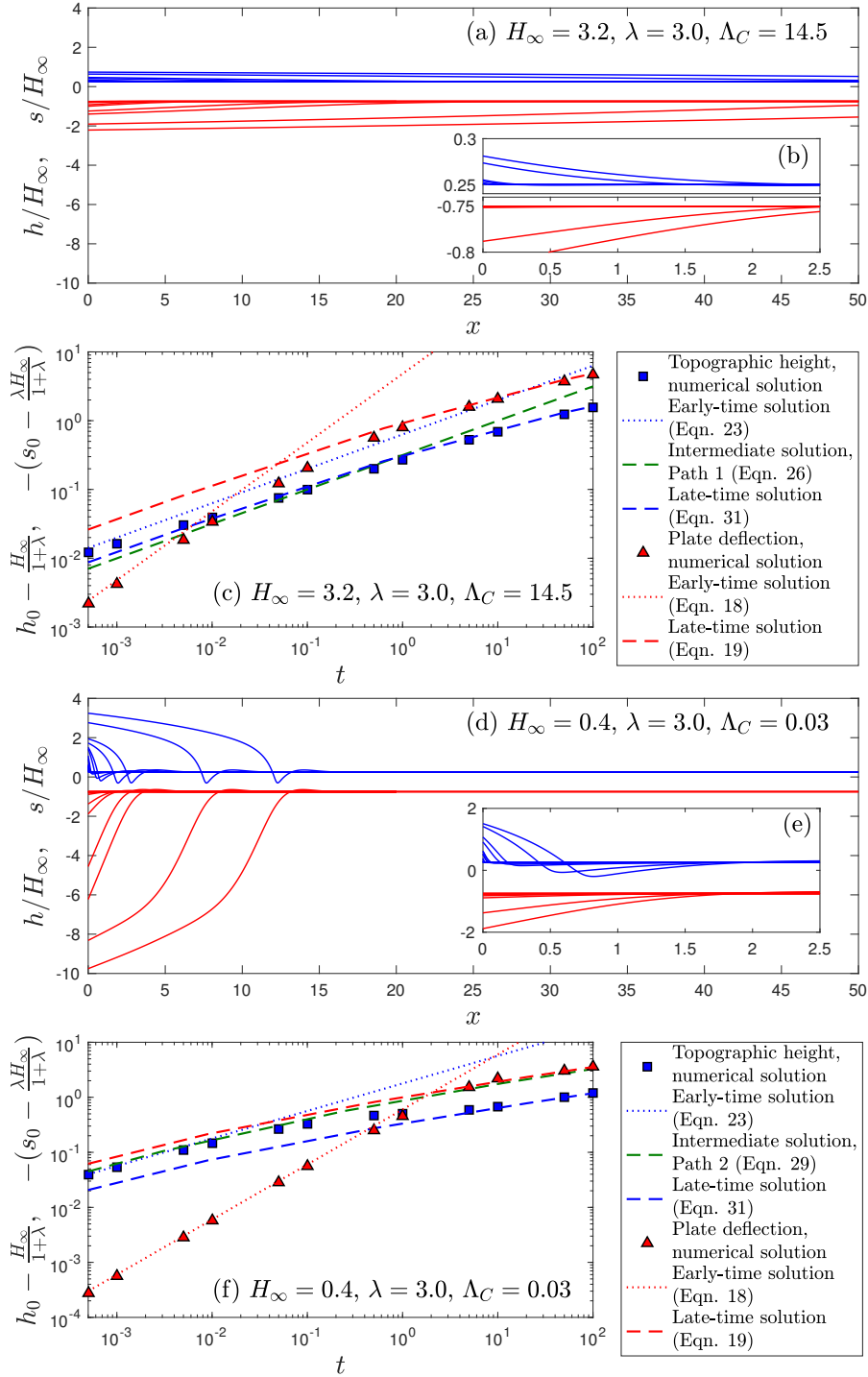
Figure 3. (a) Plot of profiles of the topographic height (blue lines) and plate deflection (red lines) for a wedge evolving along Path 1 with parameters $H_\infty = 3.2$, $\lambda = 3.0$, $\Lambda_C = 14.5$ for $t = 5 \times 10^{-4}$, $10^{-3}...10^2$, where (b) (inset) is a zoom in of profiles at early times for $t \le 10^{-1}$. (c) Log-log plot of the maximum topographic height h_0 (blue squares) and maximum plate deflection s_0 (red triangles) against time for each profile shown in (a–b). The dotted and dashed lines plot the early- and late-time solutions respectively for the maximum topographic height (blue) and the maximum plate deflection (red). The intermediate solution is given by the green dashed line. See legend for more details. (d–f) Same as (a–c) but for evolution along Path 2 with parameters $H_\infty = 0.4$, $\lambda = 3.0$, $\Lambda_C = 0.03$, where (e) (inset) is a zoom in of profiles at early times for $t \le 1$.
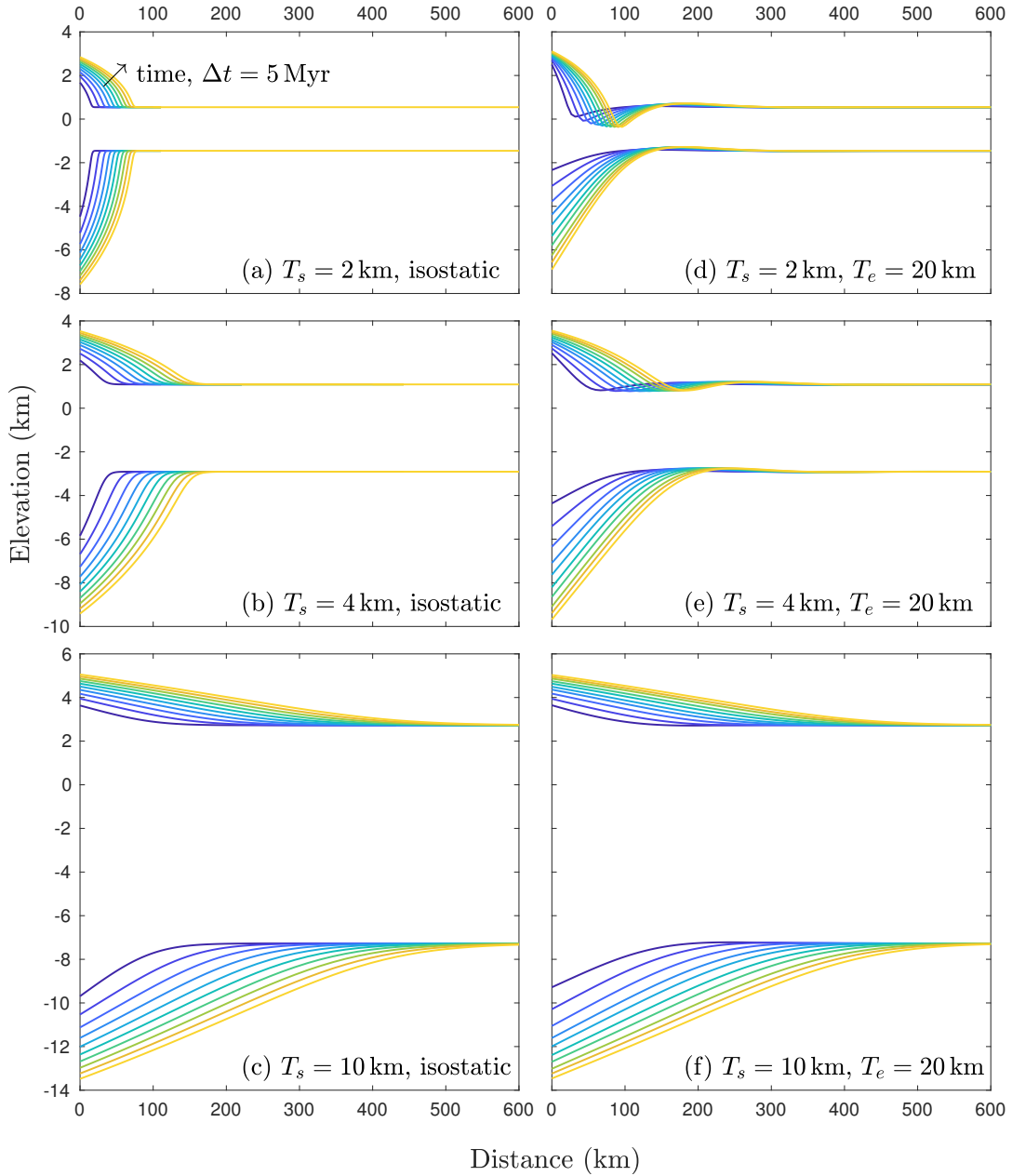
Figure 4. Dimensional plot of the growth of a fold-thrust belt considering the effects of increasing sediment thickness T_s and elastic thickness T_e. (a–c) Evolution of a wedge for $t = 5 - 50\,\mathrm{Myr}$ and sediment thicknesses $T_s = 2,\, 4,\, 10\,\mathrm{km}$ respectively in isostatic balance with no elastic thickness ($T_e = 0\,\mathrm{km}$). (d–f) Evolution of a wedge with the same sediment thicknesses as plots (a–c) but with elastic thickness $T_e = 20\,\mathrm{km}$ (Young's modulus $E = 10^{11}\,\mathrm{Pa}$, Poisson's ratio $\nu = 0.25$). In both cases, all other parameters remain the same with convergence velocity $U = 4\,\mathrm{mm\,yr^{-1}}$, viscosity $\eta = 10^{20}\,\mathrm{Pa\,s}$, sediment and underlying mantle densities $\rho = 2400\,\mathrm{kg\,m^{-3}}$, $\rho_m = 3300\mathrm{kg\,m^{-3}}$.
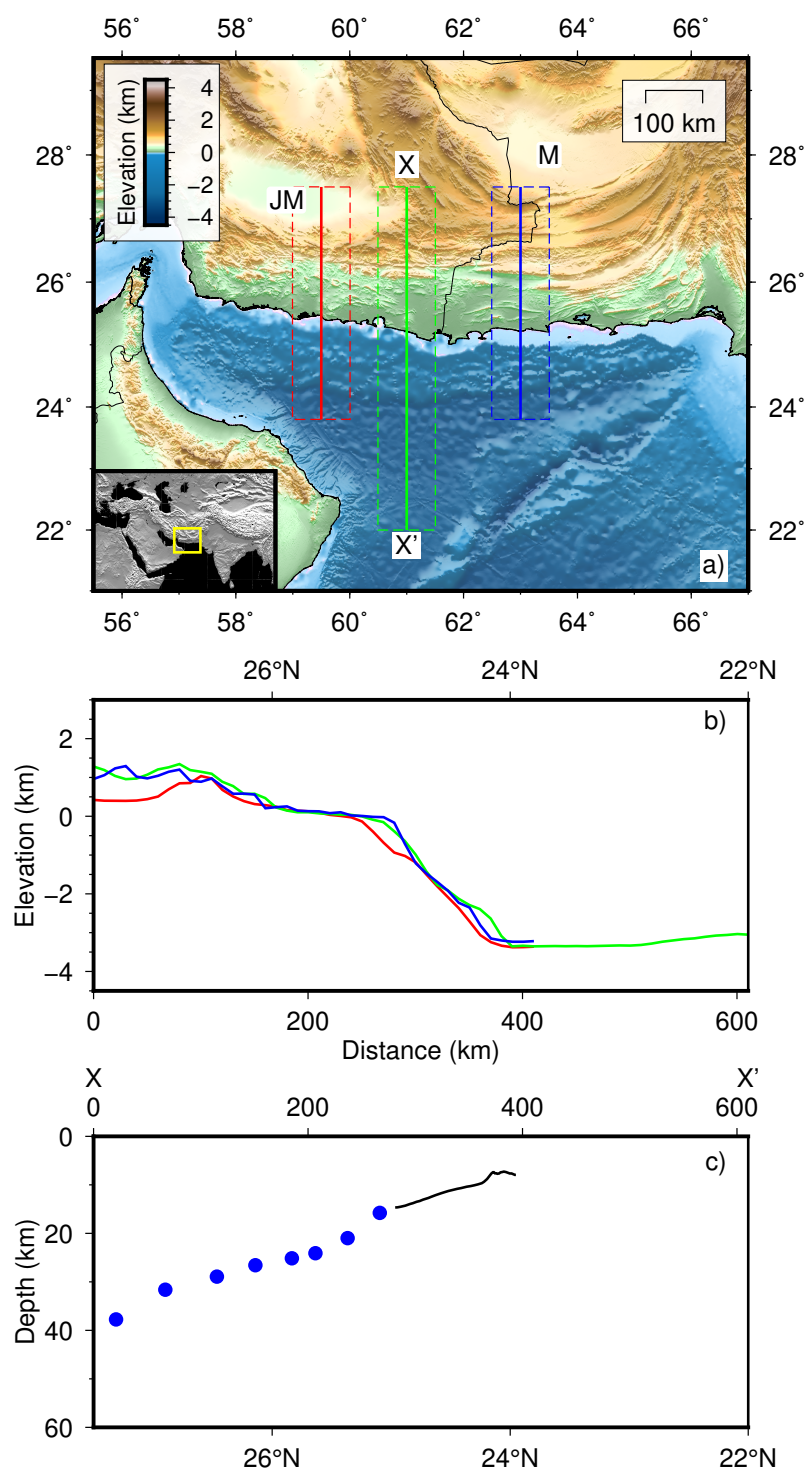
Figure 5. (a) Map of the Makran with cross sections at 59.5°E, 61°E and 63°E marked by red, green and blue boxes respectively. Dashed lines indicate the region over which profile is averaged. The Jaz Murian and Maskel depressions are marked by 'JM' and 'M'. (b) Averaged topographic profiles using a 10 km Gaussian filter plotted from north to south. (c) Sediment-basement interface from seismic reflection data at 62.9°E (solid black line, Kopp et al. 2000) and inferred subduction interface at 62°E Penney et al. (2017) based on the location of earthquakes interpreted as occurring on the subduction interface or within the subducting plate (blue dots).
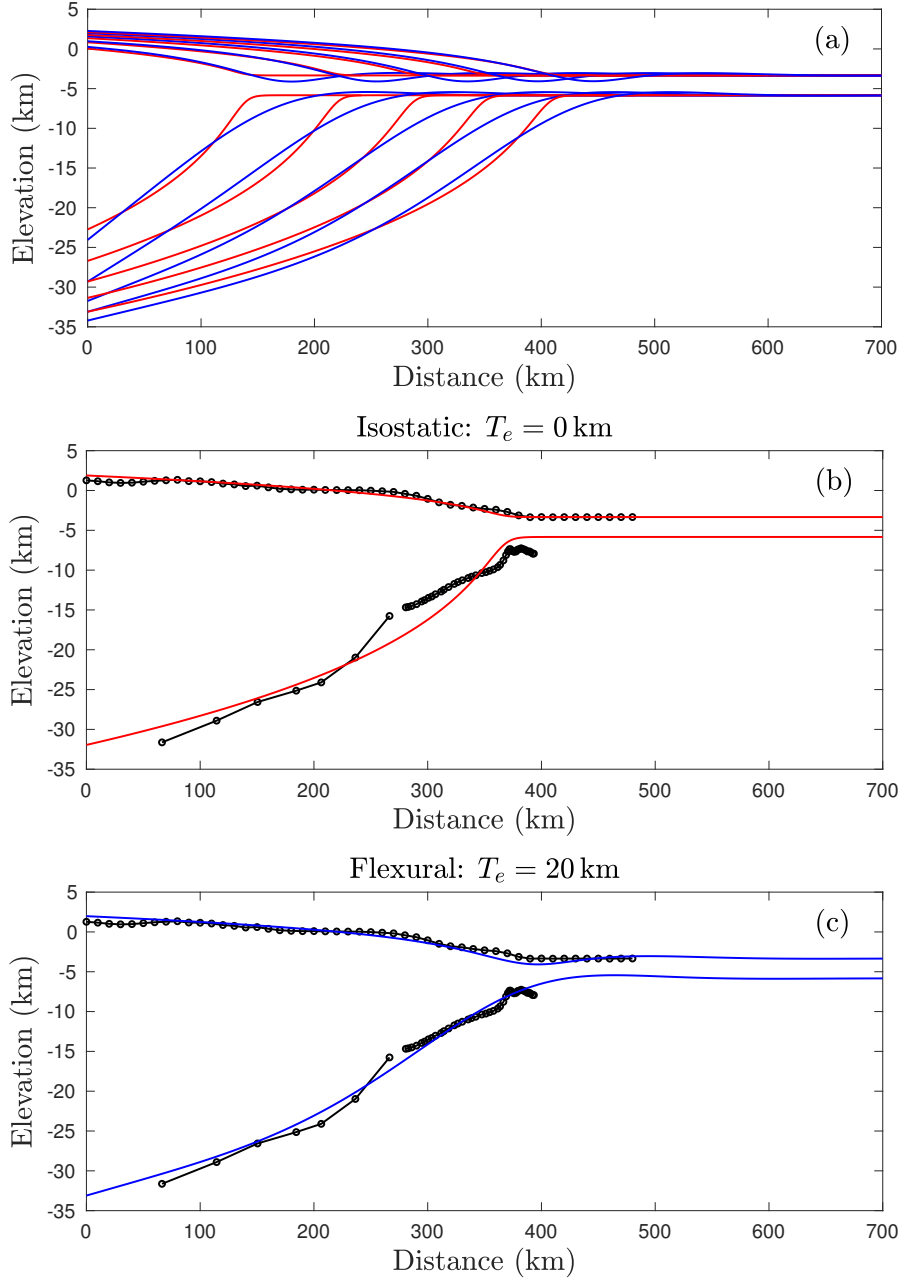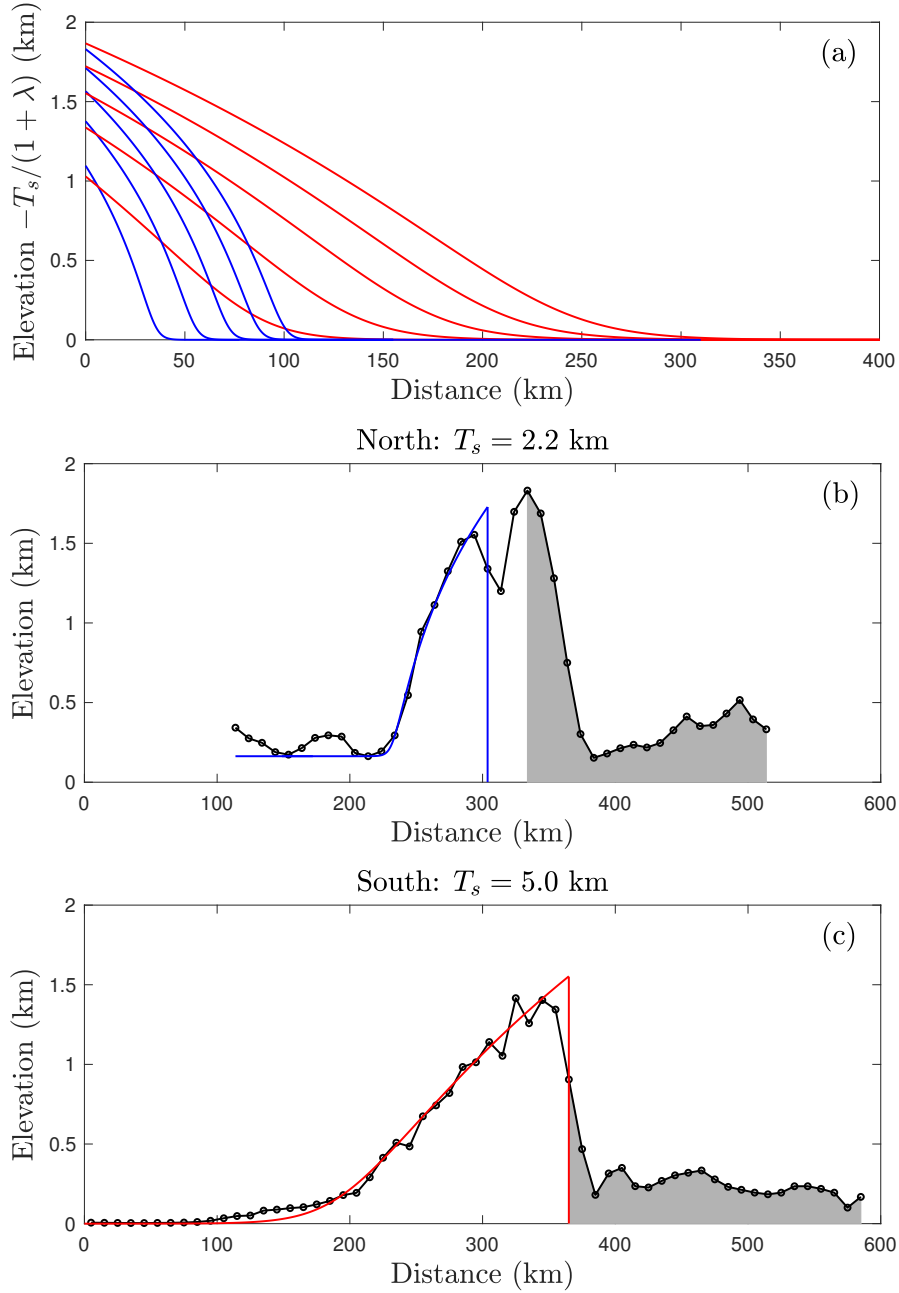
Figure 6. (a) Numerical profiles of the topography and sediment-basement interface for isostatic model with $T_e = 0\,\mathrm{km}$ (red lines) and flexural model with $T_e = 20\,\mathrm{km}$ (blue lines) for $t = 10, 20, 30, 40$ and $50\,\mathrm{Myr}$. (Sediment thickness $T_s = 7\,\mathrm{km}$, convergence velocity $U = 25\,\mathrm{mm\,yr^{-1}}$, viscosity $\eta = 1.1 \times 10^{20}\,\mathrm{Pas}$, and sediment and underlying mantle densities $\rho = 2750\,\mathrm{kg\,m^{-3}}$, $\rho_m = 3300\,\mathrm{kg\,m^{-3}}$, density ratio $\lambda = 5.0$). (b) Isostatic model with $T_e = 0\,\mathrm{km}$ for $t = 42\,\mathrm{Myr}$ (red line) plotted against data for topography and sediment-basement interface (solid black line with open circles). (c) Flexural model with $T_e = 20\,\mathrm{km}$ for $t = 42\,\mathrm{Myr}$ (blue line) plotted against data for topography and sediment-basement interface (solid black line with open circles).
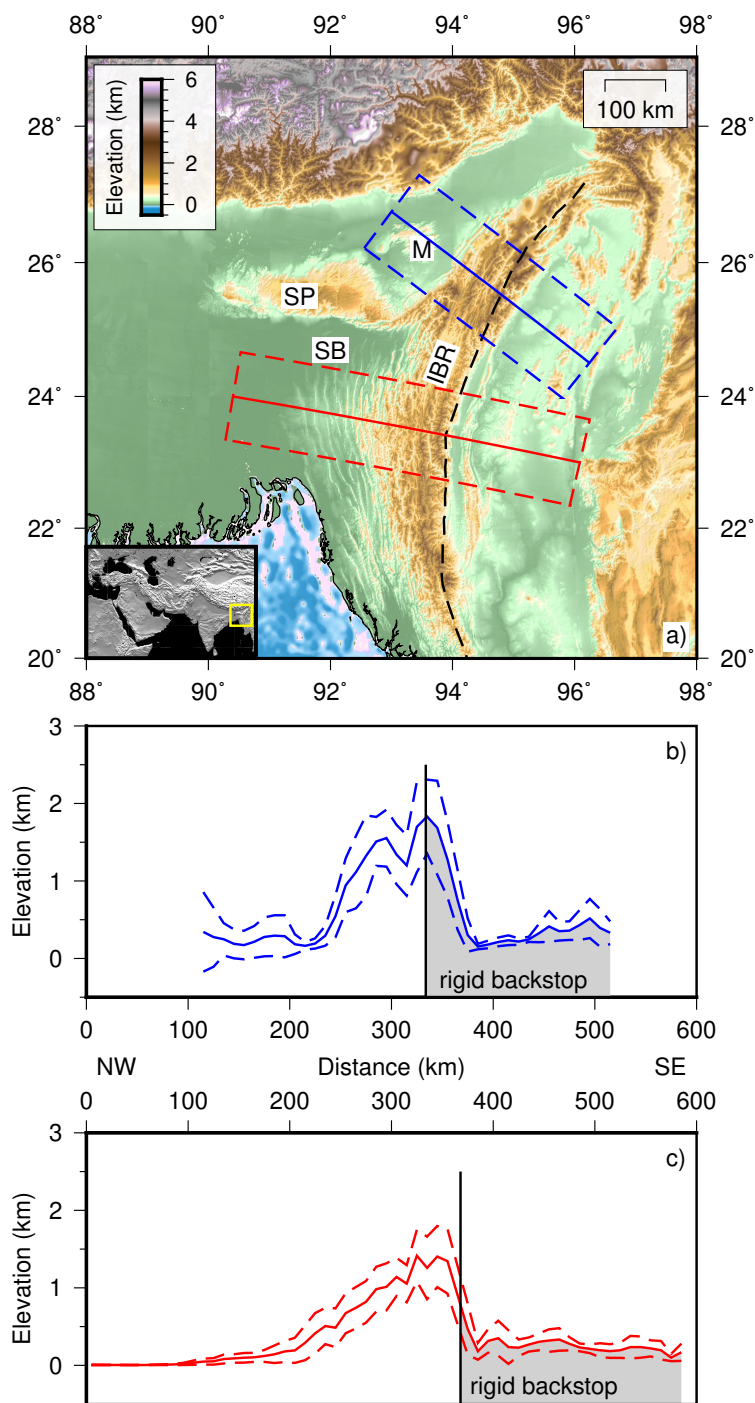
Figure 7. (a) Map of the Indo-Burman Ranges with cross-sections through the northern (blue line) and southern (red line) portion of the range. Dashed lines indicate the region over which the profile is averaged. The Shillong Plateau is marked by 'SP', the Mikir Hills by 'M', and the Surma Basin by 'SB'. Estimate of location of the backstop given by the black dashed line. (b) Averaged topographic profile using a 10 km Gaussian filter along the northern cross-section (blue line) with error bar of one standard deviation. Grey shaded area indicates estimate of the backstop. (c) Same as (b) for the southern cross-section.

Figure 8. (a) Numerical profiles of the topography for sediment thicknesses $T_{s(north)} = 2.2$ km (solid blue lines) and $T_{s(south)} = 5.0$ km (solid red lines) for $t = 10, 20, 30, 40$ and 50 Myr. (Convergence velocity $U = 3.8$ mm yr^{-1}, viscosity $\eta = 5.0 \times 10^{19}$ Pa s, and sediment and underlying mantle densities $\rho = 2400$ kg m^{-3}, $\rho_m = 3300$ kg m^{-3}, density ratio $\lambda = 2.7$). (b) Numerical profile with $T_{s(north)} = 2.2$ km for $t = 30$ Myr (solid blue line) plotted against topographic data for northern cross section of Indo-Burman Range (solid black line with open circles). (c) Numerical profile with $T_{s(south)} = 5.0$ km for $t = 30$ Myr (solid red line) plotted against topographic data for southern cross section of Indo-Burman Range (solid black line with open circles). All models are in isostatic balance with $T_e = 0$ km.

REFERENCES

M. Alam, M. M. Alam, J. R. Curray, M. L. R. Chowdhury, and M. R. Gani. An Overview of the Sedimentary Geology of the Bengal Basin in Relation to the Regional Tectonic Framework and Basin-Fill History. *Sedimentary Geology*, 155(3-4):179–208, 2003.

C. Beaumont, R. A. Jamieson, M. H. Nguyen, and B. Lee. Himalayan Tectonics Explained by Extrusion of a Low-Viscosity Crustal Channel Coupled to Focused Surface Denudation. *Nature*, 414 (6865):738–742, 2001.

P. M. Betka, L. Seeber, S. N. Thomson, M. S. Steckler, R. Sincavage, and C. Zoramthara. Slip-partitioning above a shallow, weak décollement beneath the Indo-Burman accretionary prism. *Earth and Planetary Science Letters*, 508:17–28, 2018.

R. I. Borja and S. J. Dreiss. Numerical Modeling of Accretionary Wedge Mechanics: Application to the Barbados Subduction Problem. *Journal of Geophysical Research*, 94(B7):9323–9339, 1989.

W. F. Brace and D. L. Kohlstedt. Limits on Lithospheric Stress Imposed by Laboratory Experiments. *Journal of Geophysical Research: Solid Earth*, 85(B11):6248–6252, 1980.

R. O. Brunnschweiler. On the Geology of the Indo-Burman Ranges. *Journal of the Geological Society of Australia*, 13:137–194, 1966.

R. O. Brunnschweiler. Indo-Burman Ranges. *Geological Society, London, Special Publications*, 4: 279–299, 1974.

E. V. Burov, M. G. Kogan, H. Lyon-Caen, and P. Molnar. Gravity Anomalies, the Deep Structure, and Dynamic Processes Beneath the Tien Shan. *Earth and Planetary Science Letters*, 96:367–383, 1990.

D. E. Byrne, L. R. Sykes, and D. M. Davis. Great Thrust Earthquakes and Aseismic Slip Along the Plate Boundary of the Makran Subduction Zone. *Journal of Geophysical Research*, 97(B1):449–478, 1992.

W. M. Chapple. Mechanics of Thin-Skinned Fold-and-Thrust Belts. *Bulletin of the Geological Society of America*, 89(8):1189–1198, 1978.

B. Chen, M. K. Kaban, S. E. Khrepy, and N. Al-Arifi. Effective Elastic Thickness of the Arabian Plate: Weak Shield Versus Strong Platform. *Geophysical Research Letters*, 42(2):7623–7932, 2015.

W.-P. Chen and P. Molnar. Focal Depths of Intracontinental and Intraplate Earthquakes and their Implications for the Thermal and Mechanical Properties of the Lithosphere. *Journal of Geophysical Research*, 88(B5):4183–4214, 1983.

J. A. D. Connolly and Y. Y. Podladchikov. Temperature-Dependent Viscoelastic Compaction and Compartmentalization in Sedimentary Basins. *Tectonophysics*, 324(3):137–168, 2000.

A. Copley and D. McKenzie. Models of Crustal Flow in the India-Asia Collision Zone. *Geophysical Journal International*, 169(2):683–698, 2007.

T. J. Craig and A. Copley. An Explanation for the Age Independence of Oceanic Elastic Thickness Estimates from Flexural Profiles at Subduction Zones, and Implications for Continental Rheology.

831   *Earth and Planetary Science Letters*, 392:207–216, 2014.

832   J. R. Curray. Possible Greenschist Metamorphism at the Base of a 22-km Sedimentary Section, Bay

833   of Bengal. *Geology*, 19(11):1097–1100, 1991.

834   F. Dahlen. Critical Taper Model Of Fold-And-Thrust Belts And Accretionary Wedges. *Annual Review*

835   *of Earth and Planetary Sciences*, 18(1):55–99, 1990.

836   F. A. Dahlen. Noncohesive Critical Coulomb Wedges: An Exact Solution. *Journal of Geophysical*

837   *Research: Solid Earth*, 89(B12):10125–10133, 1984.

838   F. A. Dahlen, J. Suppe, and D. Davis. Mechanics of Fold-and-Thrust Belts and Accretionary Wedges:

839   Cohesive Coulomb Theory. *Journal of Geophysical Research: Solid Earth*, 89(B12):10087–10101,

840   1984.

841   S. Dasgupta, P. Narula, S. Acharyya, and J. Banerjee. *Seismotectonic Atlas of India and its Environs*.

842   Geological Survey of India, 2000.

843   D. Davis, J. Suppe, and F. A. Dahlen. Mechanics of Fold-and-Thrust Belts and Accretionary Wedges.

844   *Journal of Geophysical Research*, 88(B2):1153–1172, 1983.

845   A. Dolati. Stratigraphy, Structural Geology and Low-Temperature Thermochronology Across the

846   Makran Accretionary Wedge in Iran. *PhD thesis*, Swiss Institute of Technology Zurich, Switzerland,

847   2010.

848   D. Elliot. The Motion of Thrust Sheets. *Journal of Geophysical Research*, 81(5):949–963, 1976.

849   S. Ellis, P. Fullsack, and C. Beaumont. Oblique Convergence of the Crust Driven by Basal Forcing:

850   Implications for Length-Scales of Deformation and Strain Partitioning in Orogens. *Geophysical*

851   *Journal International*, 120(1):24–44, 1995.

852   S. H. Emerman and D. L. Turcotte. A Fluid Model for the Shape of Accretionary Wedges. *Earth*

853   *and Planetary Science Letters*, 63(3):379–384, 1983.

854   P. England and D. McKenzie. A Thin Viscous Sheet Model for Continental Deformation. *Geophysical*

855   *Journal of the Royal Astronomical Society*, 53(9):1689–1699, 1982.

856   L. Flesch, R. Bendick, and S. Bischoff. Limitations on Inferring 3D Architecture and Dynamics From

857   Surface Velocities in the India-Eurasia Collision Zone. *Geophysical Research Letters*, 45:1379–1386,

858   2018.

859   D. W. Forsyth. Subsurface Loading and Estimates of the Flexural Rigidity of Continental Lithosphere.

860   *Journal of Geophysical Research*, 90(B14):12623–12632, 1985.

861   N. C. Ghose and R. N. Singh. Occurrence of Blueschist Facies in the Ophiolite Belt of Naga Hills,

862   East of Kiphire, N. E. India. *Geologische Rundschau*, 69:41–48, 1980.

863   G. Govin, Y. Najman, A. Copley, I. Millar, P. van der Beek, P. Huyghe, D. Grujic, and J. Davenport.

864   Timing and Mechanism of the Rise of the Shillong Plateau in the Himalayan Foreland. *Geology*, 46

865   (3):279–282, 2018.

866   J.-P. Gratier, F. Renard, and P. Labaume. How Pressure Solution Creep and Fracturing Processes

867   Interact in the Upper Crust to Make it Behave in Both a Brittle and Viscous Manner. *Journal of*

Structural Geology, 21(8-9):1189–1197, 1999.

J. Gratton and C. A. Perazzo. Self-Similar Asymptotics in Convergent Viscous Gravity Currents of Non-Newtonian Liquids. *Journal of Physics: Conference Series*, 166:012011, 2009.

D. Haddad and A. B. Watts. Subsidence History, Gravity Anomalies, and Flexure of the Northeast Australian Margin in Papua New Guinea. *Tectonics*, 18(5):827–842, 1999.

T. A. Jordan and A. B. Watts. Gravity Anomalies, Flexure and the Elastic Thickness Structure of the India-Eurasia Collisional System. *Earth and Planetary Science Letters*, 236(3-4):732–750, 2005.

G. D. Karner and A. B. Watts. Gravity Anomalies and Flexure of the Lithosphere at Mountain Ranges. *Journal of Geophysical Research: Solid Earth*, 88(B12):10449–10477, 1983.

C. Kopp, J. Fruehn, E. R. Flueh, C. Reichert, N. Kukowski, J. Bialas, and D. Klaeschen. Structure of the Makran Subduction Zone from Wide-Angle and Reflection Seismic Data. *Tectonophysics*, 329 (1-4):171–191, 2000.

K. Khin, T. Sakai, and K. Zaw. Neogene Syn-Tectonic Sedimentation in the Eastern Margin of Arakan-Bengal Basins, and its Implications on for the Indian-Asian Collision in Western Myanmar. *Gondwana Research*, 26(1):89–111, 2014.

K. Khin, T. Sakai, and K. Zaw. Arakan Coastal Ranges in Western Myanmar, Geology and Provenance of Neogene Siliciclastic Sequences: Implications for the Tectonic Evolution of the Himalaya-Bengal System. *Geological Society, London, Memoir*, 48:81–116, 2017.

N. Kukowski, T. Schillhorn, K. Huhn, U. von Rad, S. Husen, and E. R. Flueh. Morphotectonics and Mechanics of the Central Makran Accretionary Wedge Off Pakistan. *Marine Geology*, 173(1-4):1–19, 2001.

H. Lyon-Caen and P. Molnar. Constraints on the Structure of the Himalaya from an Analysis of Gravity Anomalies and a Flexural Model of the Lithosphere. *Journal of Geophysical Research*, 88 (B10):8171–8191, 1983.

G. Mandl. Mechanics of Tectonic Faulting: Models and Basic Concepts. *Developments in Structural Geology, 1*, 1:407, 1988.

D. McKenzie and D. Fairhead. Estimates of the Effective Elastic Thickness of the Continental Lithosphere from Bouguer and Free Air Gravity Anomalies. *Journal of Geophysical Research: Solid Earth*, 102(B12):27523–27552, 1997.

B. J. Meade. Present-Day Kinematics at the India-Asia Collision Zone. *Geology*, 35(1):81–84, 2007.

S. Medvedev. Mechanics of Viscous Wedges: Modeling by Analytical and Numerical Approaches. *Journal of Geophysical Research*, 107(B6):2123, 2002.

A. H. G. Mitchell. Cretaceous-Cenozoic Tectonic Events in the Western Myanmar (Burma)-Assam Region. *Journal of the Geological Society, London*, 150(6):1089–1102, 1993.

P. Molnar and P. Tapponnier. Cenozoic Tectonics of Asia: Effects of a Continental Collision. *Science*, 189(4201):419–426, 1975.

J. F. Ni, M. Guzman-Speziale, M. Bevis, W. E. Holt, T. C. Wallace, and W. R. Seager. Accretionary

Tectonics of Burma and the Three-Dimensional Geometry of the Burma Subduction Zone. *Geology*, 17(1):68–71, 1989.

F. Nino, J. Chéry, and J.-P. Gratier. Mechanical Modeling of Compressional Basins: Origin and Interaction of Faults, Erosion, and Subsidence in the Ventura basin, California. *Tectonics*, 17(6): 955–972, 1998.

C. Penney, F. Tavakoli, A. Saadat, H. R. Nankali, M. Sedighi, F. Khorrami, F. Sobouti, Z. Rafi, A. Copley, J. Jackson, and K. Priestley. Megathrust and Accretionary Wedge Properties and Behaviour in the Makran Subduction Zone. *Geophysical Journal International*, 209(3):1800–1830, 2017.

C. A. Perazzo and J. Gratton. Asymptotic Regimes of Ridge and Rift Formation in a Thin Viscous Sheet Model. *Physics of Fluids*, 20(4):043103, 2008.

C. A. Perazzo and J. Gratton. Convergent Flow in a Two-Layer System and Mountain Building. *Physics of Fluids*, 22(5):056603, 2010.

J. P. Platt, J. K. Leggett, J. Young, H. Raza, and S. Alam. Large-Scale Sediment Underplating in the Makran Accretionary Prism, Southwest Pakistan. *Geology*, 13(7):507–511, 1985.

R. A. Price. Large-Scale Gravitational Flow of Supra-Crustal Rocks, Southern Canadian Rockies. *Gravity and Tectonics*, pages 491–502, 1973.

J. B. Ruh, B. J. Kaus, and J. P. Burg. Numerical Investigation of Deformation Mechanics in Fold-and-Thrust Belts: Influence of Rheology of Single and Multiple Décollements. *Tectonics*, 31(3):1–23, 2012.

E. H. Rutter. Pressure Solution in Nature, Theory and Experiment. *Journal of the Geological Society*, 140:725–740, 1983.

H. Schlichting and A. H. Shapiro. *Boundary-Layer Theory 7th ed.* McGraw-Hill, 1979.

R. L. Shreve and M. Cloos. Dynamics of Sediment Subduction, Melange Formation, and Prism Accretion. *Journal of Geophysical Research*, 91(B10):10229–10245, 1986.

A. M. Sikder and M. M. Alam. 2-D Modelling of the Anticlinal Structures and Structural Development of the Eastern Fold Belt of the Bengal Basin, Bangladesh. *Sedimentary Geology*, 155(3-4):209–226, 2003.

G. D. H. Simpson. Influence of the Mechanical Behaviour of Brittle-Ductile Fold-Thrust Belts on the Development of Foreland Basins. *Basin Research*, 22(2):139–156, 2010.

G. D. H. Simpson. Mechanics of Non-Critical Fold-Thrust Belts Based on Finite Element Models. *Tectonophysics*, 499(1-4):142–155, 2011.

G. D. H. Simpson. Modelling Interactions Between Fold-Thrust Belt Deformation, Foreland Flexure and Surface Mass Transport. *Basin Research*, 18(2):125–143, 2006.

D. B. Snyder and M. Barazangi. Deep Crustal Structure and Flexure of the Arabian Plate Beneath the Zagros Collisional Mountain Belt as Inferred from Gravity Observations. *Tectonics*, 5(3):361–373, 1986.

I. Soibam, M. C. Khuman, and S. S. Subhamenon. Ophiolitic Rocks of the Indo-Myanmar Ranges, NE India: Relicts of an Inverted and Tectonically Imbricated Hyper Extended Continental Margin Basin? *Geological Society, London, Special Publications*, 413, 2015.

M. S. Steckler, S. H. Akhter, and L. Seeber. Collision of the Ganges-Brahmaputra Delta with the Burma Arc: Implications for Earthquake Hazard. *Earth and Planetary Science Letters*, 273(3-4): 367–378, 2008.

M. S. Steckler, D. R. Mondal, S. H. Akhter, L. Seeber, L. Feng, J. Gale, E. M. Hill, and M. Howe. Locked and Loading Megathrust Linked to Active Subduction Beneath the Indo-Burman Ranges. *Nature Geoscience*, 9(8):615–618, 2016.

G. S. Stockmal. Modeling of Large-Scale Accretionary Wedge Deformation. *Journal of Geophysical Research*, 88(B10):8271–8287, 1983.

G. S. Stockmal, C. Beaumont, M. H. Nguyen, and B. Lee. Mechanics of Thin-Skinned Fold-and-Thrust Belts: Insights from Numerical Models. *Geological Society of America*, 433:63–98, 2007.

A. L. Stork, N. D. Selby, R. Heyburn, and M. P. Searle. Accurate Relative Earthquake Hypocenters Reveal Structure of the Burma Subduction Zone. *Bulletin of the Seismological Society of America*, 98(6):2815–2827, 2008.

J. Suppe. A Retrodeformable Cross Section of Northern Taiwan. *Proceedings of the Geological Society of China*, 23:46–55, 1980.

S. Mitra, K. Priestley, A. K. Bhattacharyya, and V. K. Gaur Crustal Structure and Earthquake Focal Depths Beneath Northeastern India and Southern Tibet. *Geophysical Journal International*, 160(1): 227-248, 2005.

S. Timoshenko and S. Woinowsky-Krieger. *Theory of Plates and Shells.* McGraw-Hill, 1959.

P. Vernant, F. Nilforoushan, D. Hatzfeld, M. R. Abbassi, C. Vigny, F. Masson, H. Nankali, J. Martinod, A. Ashtiani, R. Bayer, F. Tavakoli, and J. Chéry. Present-Day Crustal Deformation and Plate Kinematics in the Middle East Constrained by GPS Measurements in Iran and Northern Oman. *Geophysical Journal International*, 157(1):381–398, 2004.

R. I. Walcott. Flexural Rigidity, Thickness, and Viscosity of the Lithosphere. *Journal of Geophysical Research*, 75(20):3941–3954, 1970.

W.-H. Wang. Lithospheric Flexure Under a Critically Tapered Mountain Belt: a New Technique to Study the Evolution of the Tertiary Taiwan Orogeny. *Earth and Planetary Science Letters*, 192(4): 571–581, 2001.

K. Wang, and Y. Hu. Accretionary Prisms in Subduction Earthquake Cycles:The Theory of Dynamic Coulomb Wedge. *Journal of Geophysical Research*, 111(B06410):2006.

A. B. Watts, S. H. Lamb, J. D. Fairhead, and J. F. Dewey. Lithospheric Flexure and Bending of the Central Andes. *Earth and Planetary Science Letters*, 134(1-2):9–21, 1995.

A. B. Watts, S. J. Zhong, and J. Hunter. The Behavior of the Lithosphere on Seismic to Geologic Timescales. *Annual Review of Earth and Planetary Sciences*, 41:443–468, 2013.

979   R. S. White. Deformation of the Makran Accretionary Sediment Prism in the Gulf of Oman (North-
980   West Indian Ocean). *Geological Society, London, Special Publications*, 10:357–372, 1982.

981   S. D. Willett. Dynamic and Kinematic Growth and Change of a Coulomb Wedge. *Thrust Tectonics*,
982   pages 19–31, 1992.

983   W.-L. Zhao, D. M. Davis, F. A. Dahlen, and J. Suppe. Origin of Convex Accretionary Wedges:
984   Evidence from Barbados. *Journal of Geophysical Research*, 91(B10):10246–10,258, 1986.